International Journal of Heat and Mass Transfer 271 (2026) 129395

Contents lists available at ScienceDirect

International Journal of Heat and Mass Transfer

journal homepage: www.elsevier.com/locate/hmt

Direct numerical simulation study of the effect of horizontal flow on mixed convection in porous media

Yan Jin *, Arne Speerforck

Institute of Engineering Thermodynamics, Hamburg University of Technology, Hamburg, 21073, Germany

ARTICLE INFO

Keywords:
Porous medium
Mixed convection
Direct numerical simulation
Nusselt number
Instability
Dispersion

ABSTRACT

A direct numerical simulation (DNS) study is performed on mixed convection in a chamber filled with a porous medium composed of staggered circular elements. Natural convection is driven by a temperature difference between the two walls, while forced convection is caused by a prescribed horizontal force. The Rayleigh number in the range $1000 \leq Ra \leq 20000$, pore-scale Rayleigh number in the range $1.2 \leq Ra_K \leq 39.2$, Peclet–Rayleigh number ratio in the range $0 \leq Pe_K/Ra_K \leq 1$, Prandtl number $Pr = 250$, and porosity $\phi = 0.46$ and 0.56 are considered in the DNS study. The DNS results reveal that pore-scale dispersion caused by natural convection is significant due to the large Ra_K. It enhances the merging of small plumes in the boundary layer and reduces the mega-plume number. The horizontal flow has two competing effects on heat transfer. It weakens vertical macroscopic advection and pore-scale dispersion, and thus reduces the heat transfer. However, it also weakens small-scale horizontal motions in the boundary layer, which prevents the mega-plumes from merging and enhances the heat transfer. Consequently, the mega-plume number increases at $Ra = 1000$ as Pe_K/Ra_K rises from 0 to 1. At $Ra = 20000$, the mega-plume number increases as Pe_K/Ra_K increases from 0 to 0.1; however, it decreases as Pe_K/Ra_K increases to 1, due to strong dispersion caused by the horizontal flow. The overall effect of the horizontal flow is mainly to reduce the Nusselt number. The Nusselt number follows the scaling law $Nu \sim Ra^a$, where a can be approximated as $a = 0.5 - 2.5 \times 10^{-6} Pe$ for the present DNS cases.

1. Introduction

In porous media, convection is the process by which heat or mass is transferred due to fluid motion within the pore spaces. This essential phenomenon takes place in many engineering and natural systems, including groundwater transport [1], CO_2 sequestration in deep saline aquifer [2], oil refineries [3], geothermal energy extraction [4], and heat exchangers [5], etc.

Convection can be classified as either forced convection, which is driven by an external force, or natural convection, which is driven by density variations caused by temperature or concentration changes. In some cases, both forced and natural convection play important roles, resulting in mixed convection in porous media. Examples include heat exchangers, enhanced geothermal reservoirs used for heat extraction, and enhanced oil recovery. In these cases, the injected fluid creates forced convection, and the temperature gradient creates a buoyancy force. The interaction between these two forces leads to mixed convection.

In recent years, mixed convection in porous media has received increasing attention due to its important applications. Corresponding studies have often been performed for specific applications. For instance, external mixed convection induced by heating a vertical plane wall [6], tube [7,8] or sphere [9,10] is studied to understand the process of geothermal energy extraction. Internal mixed convection in a horizontal [11,12] or vertical channel [13] is studied to understand the processes in heat exchangers or thermal storage systems.

An important objective of these studies is to predict the Nusselt number (Nu) for convection. The Nusselt number correlation has already been extensively studied when heat transfer is purely determined by forced convection. For a flat surface bordering a fluid-saturated porous medium, it was found that the Nusselt number follows the scaling law $Nu \sim Pe_x^{1/2}$, where Pe_x is the Peclet number defined using the length of the heating section x as the characteristic length. For heat transfer around a circular cylinder or a sphere, the scaling law of the Nusselt number becomes $Nu \sim Pe_D^{1/2}$ where Pe_D is the Peclet number defined using the cylinder/sphere diameter D. Both x and D are macroscopic lengths. In fully developed forced convection in a channel or a pipe, the effect of Pe_x or Pe_D disappears and Nu becomes a constant, i.e., $Nu = c$. In a tube filled with a porous medium, c has the values of 5.78 for a constant wall temperature and 8 for

* Corresponding author.
E-mail address: yan.jin@tuhh.de (Y. Jin).

https://doi.org/10.1016/j.ijheatmasstransfer.2026.129395
Received 19 February 2026; Received in revised form 10 July 2026; Accepted 5 August 2026
Available online 13 August 2026

Nomenclature

Roman letters

$\hat{u}'$	Horizontal-line, REV- and time-averaged r.m.s. horizontal velocity, $\mathrm{m\,s^{-1}}$
$\hat{v}'$	horizontal-line, REV- and time-averaged r.m.s. vertical velocity, $\mathrm{m\,s^{-1}}$
$\hat{x}_i$	Cartesian coordinate for the macroscopic field, m
$\hat{y}$	Vertical Cartesian coordinate for the macroscopic field, –
a	Scaling coefficient, –
a_i	Prescribed horizontal acceleration rate $a\delta_{i1}$, $\mathrm{m\,s^{-2}}$
d	Circular element diameter, m
Da	Darcy number, –
g_i	Prescribed gravitational acceleration rate $-g\delta_{i2}$, $\mathrm{m\,s^{-2}}$
H	Domain height, m
K	Permeability, $\mathrm{m^2}$
L	Domain width, m
N_{REV}	Number of mesh cells to resolve an REV, –
Nu	Nusselt number, –
Pe_K	Pore-scale Peclet number, –
Pr	Prandtl number ν/α, –
Ra	Rayleigh number, -
Ra_K	Pore-scale Rayleigh number, –
t	Time, s
T_h	High temperature, K
T_l	Low temperature, K
u_F	Characteristic velocity for forced convection, $\mathrm{m\,s^{-1}}$
u_i	Velocity component, $\mathrm{m\,s^{-1}}$
u_N	Characteristic velocity for natural convection, $\mathrm{m\,s^{-1}}$
x_i	Cartesian coordinate, m

Greek symbols

α	Thermal diffusion coefficient, $\mathrm{m^2\,s^{-1}}$
α_e	Effective thermal diffusion coefficient, $\mathrm{m^2\,s^{-1}}$
α_l	Longitudinal thermal dispersion coefficient, $\mathrm{m^2\,s^{-1}}$
α_t	Transverse thermal dispersion coefficient, $\mathrm{m^2\,s^{-1}}$
ΔT	Temperature difference $T_h - T_c$, K
Δ_c	Mesh cell size, m
Γ_i	Dimensionless macroscopic molecular diffusion vector component, –
γ_m	Thermal diffusion coefficient ratio α_e/α, –
$\hat{\theta}$	horizontal-line, REV- and time-averaged dimensionless temperature, –
ϕ	Porosity, -
Φ_i	Dimensionless macroscopic advection vector component, –
Ψ_i	Dimensionless macroscopic dispersion vector component, –
θ	Dimensionless temperature, –
θ'	r.m.s. dimensionless temperature, –

Superscripts

$\bar{\ }$	Time averaging
$\langle\rangle^i$	Averaging in the fluid portion of an REV
$\langle\rangle_x$	Horizontal averaging

Abbreviations

DNS	Direct numerical simulation
DOB	Darcy–Oberbeck–Boussinesq
REV	Representative elementary volume

a constant heat flux. In a channel filled with a porous medium, c has the values of 4.93 for a constant wall temperature and 6 for a constant heat flux. More details about these correlations can be found in [14]. Sometimes Nu needs to be corrected when the pore-scale thermal dispersion is significant. For heat transfer over a flat surface, the scaling law is $Nu \sim \left(1 + cPe_d^a\right) Pe_x^{1/2}$, where Pe_d is the pore-scale Peclet number. Lai and Kulaki suggest that the scaling coefficient a to be set to 1 [15]. However, de Lemos indicates that a decreases as the porosity ϕ decreases [16]. A recent study by Liu, et al. suggests that the longitudinal dispersion coefficient changes from a power-law scaling, to linear scaling, and eventually to logarithmic scaling as the Peclet number increases [17].

Some other studies focus on the pure natural convection while the forced convection is neglected. For internal natural convection with heat from below, Elder proposed the correlation $Nu = Ra/40$ at large Rayleigh numbers in the Darcy regime [18]. Based on the Darcy–Oberbeck–Boussinesq (DOB) simulations, Hewitt et al. suggest the linear scaling law $Nu = 9.6 \times 10^{-3} Ra + 4.6$ [19–21], while Kränzien and Jin suggest $Nu = 7.6 \times 10^{-3} Ra + 0.935$ [22]. A pore-scale resolved direct numerical simulation (DNS for short) study by Gasow et al. suggests a nonlinear scaling law $Nu = aRa^{1-0.2\phi^2} + 1$, where $a = 0.011 \pm 0.002$ is a pore-scale geometric parameter [23]. For natural convection adjacent to a heated vertical flat plate, the Nusselt number follows the scaling law $Nu \sim Ra^{1/2}$ [24]. This changes to $Nu \sim Ra^{1/3}$ for natural convection adjacent to a heated horizontal plate [25,26]. Wang and Mobedi studied natural convection involving solid–liquid phase change in a porous medium [27]. Their numerical results were compared with established correlations and showed good agreement. Xu, et al. indicated the significant impact of impermeable solid porous matrices on the statistical properties of temperature and thermal energy dissipation rate [28].

Mixed convection is often believed to be determined by both the Rayleigh number Ra and the Peclet number Pe. The ratio of these two dimensionless numbers, Ra/Pe, is sometimes referred to as the mixed convection parameter [29]. Lai and Kulacki suggest that thermal dispersion induced by forced convection can improve the heat transfer [30]. However, in another study, Combarnous and Bia suggest that the axial flow causing the forced convection does not affect the critical Rayleigh number for the onset of natural convection or the heat transfer in a rectangular duct [11]. Summarizing the previous studies, Nakayama and Pop proposed a unified theory for mixed convection. According to this theory convection in porous media is classified into six regimes, they are forced convection, Darcy natural convection, Forchheimer natural convection, Darcy mixed convection, Darcy–Forchheimer natural convection and Forchheimer mixed convection regimes [31]. According to this study, the Nusselt number (Nu) has the scaling law $Nu \sim (Pe + Ra)^{1/2}$ in the Darcy mixed convection regime. In the Forchheimer mixed convection regime, the scaling law becomes $Nu \sim (Pe + Ra)^{1/4}$.

Convection in porous media has also been studied in mass transfer problems. Emami-Meybodi suggests that, dispersion due to the horizontal velocity leads to lower Sherwood number and the critical wavenumber for instability onset [32]. However, an experimental study by Michel-Meyer shows that the horizontal velocity has no significant effect on the Sherwood number in the constant flux regime [33]. Another numerical study by Tsinober et al. shows that the natural convection dominates when $Pe/Ra < 0.77$; the forced convection dominates when $Pe/Ra > 2$. In the regime of the mixed convection $0.77 < Pe/Ra < 2$, the Sherwood number is expressed as $Sh = \left(Sh_N^n + Sh_F^n\right)^{1/n}$ [34], where Sh_N and Sh_F are the Sherwood numbers for pure natural and forced convection, respectively. Xu et al. investigated mass transfer from the bulk flow to pore surfaces in chemically reactive flows through both ordered and disordered porous structures [35]. They found that the Sherwood number increases linearly with the Reynolds number in the creeping-flow regime, whereas it exhibits a square-root dependence on the Reynolds number in the inertial-flow regime. Since the Sherwood and Nusselt numbers are similar, these studies also help us to understand mixed convection in heat transfer problems.

In addition, some studies have focused on the flow patterns and flow instabilities in mixed convection in porous media. For example, Islam demonstrates the periodic, quasi-periodic, and chaotic behavior of the plumes at high Ra [36]. Chandra indicates that the flow structure depends on the Darcy number Da, Grashof number Gr and the Reynolds number Re [12]. Chung et al. studied the onset of flow instability in mixed convection using linear and weakly nonlinear theories [37,38]. Sharma and Bera performed a linear stability analysis of the mixed convection induced by an external pressure gradient and buoyancy force due to differentially heated wall surfaces [13].

Despite the efforts of previous studies, the interaction between forced and natural convection and its influence on heat transfer remain insufficiently understood. In particular, the mechanisms by which an imposed horizontal flow modifies the buoyancy-driven plume dynamics and consequently affects the Nusselt number are still unclear. In addition, detailed information on the flow and thermal structures, including plume dynamics, r.m.s. velocity and temperature fluctuations, and pore-scale transport processes, remains limited. Such information is essential for understanding the mechanisms of mixed convection, assessing the validity of macroscopic transport models, and improving predictive correlations for heat transfer in porous media.

The purpose of this study is to better understand the mechanism of mixed convection in porous media. The crucial question is how forced convection due to horizontal flows influences macroscopic advection and pore-scale dispersion and thus affects mixed convection. To this end, a pore-scale resolved direct numerical simulation (DNS) study was performed. The paper is structured as follows. After the introduction, Section 2 describes the governing equations and numerical methods. Section 3 introduces the cases studied. Section 4 discusses the DNS results. Section 5 provides the main conclusions.

2. Mathematical equations and numerical method

2.1. Governing equations for DNS

Fig. 1 schematically demonstrates the problem studied. The computational domain is a two-dimensional cell with the height H and width $L = 2H$ filled with a porous medium consisting of staggered circular elements. High and low temperatures, T_h and T_c, are prescribed at the lower and upper boundaries, while the surfaces of the porous elements are assumed to be adiabatic. This treatment is based on the assumption that the thermal conductivity of the solid phase is negligibly small. Consequently, heat transfer within the solid phase is neglected and conjugate heat transfer is not considered in the current work. A non-slip condition is used at the upper and lower boundaries, as well as on the surfaces of the porous matrix. A periodic boundary condition is used in the horizontal direction.

A gravitational force $\rho g_i = -\rho g \delta_{i2}$ is prescribed in the vertical x_2 direction, where the density ρ depends on the temperature, leading to the buoyancy force. Another acceleration force $\rho_0 a_i = \rho_0 a \delta_{i1}$ is given in the horizontal x_1 direction, where ρ_0 is the reference density, leading to the forced convection. The fluid is assumed to be incompressible with the buoyancy force calculated using the Boussinesq approximation. The governing equations for the mass, momentum and energy conservation read

$$\frac{\partial u_i}{\partial x_i} = 0, \tag{1}$$

$$\frac{\partial u_i}{\partial t} + \frac{\partial (u_j u_i)}{\partial x_j} = -\frac{\partial p}{\partial x_i} + \nu \frac{\partial^2 u_i}{\partial x_j^2} - \beta \Delta T \theta g_i + a_i, \tag{2}$$

$$\frac{\partial \theta}{\partial t} + \frac{\partial (u_i \theta)}{\partial x_i} = \alpha \frac{\partial^2 \theta}{\partial x_i^2}, \tag{3}$$

where u_i, p, ΔT, ν, β and α are the velocity component, pressure, Temperature difference $T_h - T_c$, kinematic viscosity, thermal expansion coefficient and thermal diffusivity, respectively. The dimensionless temperature θ is defined as $\theta = \frac{T - T_c}{T_h - T_c}$.

2.2. Macroscopic equations

By averaging Eqs. (1)–(3) in each representative elementary volume (REV), which is shown in Fig. 1 and accounting for the zero heat flux at solid surfaces, we obtained the following macroscopic equations:

$$\frac{\partial \left(\phi \langle u_i \rangle^i\right)}{\partial \hat{x}_i} = 0, \tag{4}$$

$$\begin{aligned}\frac{\partial \left(\phi \langle u_i \rangle^i\right)}{\partial t} + \frac{\partial \left(\phi \left\langle u_j \right\rangle^i \langle u_i \rangle^i\right)}{\partial \hat{x}_j} + \frac{\partial \left(\phi \left\langle {}^i u_j^i u_i \right\rangle^i\right)}{\partial \hat{x}_j} = -\frac{\partial \left(\phi \langle p \rangle^i\right)}{\partial \hat{x}_i} \\ + \frac{\partial}{\partial \hat{x}_j}\left(\nu_e \frac{\partial \langle u_i \rangle^i}{\partial \hat{x}_j}\right) - \phi \beta \Delta T \langle \theta \rangle^i g_i + \phi a_i - \phi^2 \frac{\nu}{K} \langle u_i \rangle^i ,\end{aligned} \tag{5}$$

$$\frac{\partial \left(\phi \langle \theta \rangle^i\right)}{\partial t} + \frac{\partial (\phi \langle u_i \rangle^i \langle \theta \rangle^i)}{\partial \hat{x}_i} + \frac{\partial \left(\phi \left\langle {}^i u_i^i \theta \right\rangle^i\right)}{\partial \hat{x}_i} = \frac{\partial}{\partial \hat{x}_i}\left(\alpha_e \frac{\partial \langle \theta \rangle^i}{\partial \hat{x}_i}\right), \tag{6}$$

where ν_e and α_e are the effective viscosity and effective thermal diffusivity. Gasow, et al. suggest that they only depend on the fluid properties and the pore-scale geometry [39]. K is the permeability. It is assumed that the Forchheimer term can be neglected. $\hat{x}_i$ is the coordinate of the macroscopic field. The operator $\langle\rangle^i$ denotes the intrinsic volume average in the fluid phase of a REV [16]. For a scalar ψ, ${}^i\psi = \psi - \langle \psi \rangle^i$ is the residual of ψ after the volume averaging. $\phi \left\langle {}^i u_j^i u_i \right\rangle^i$ and $\phi \left\langle {}^i u_i^i T \right\rangle^i$ result in the pore-scale momentum dispersion and thermal dispersion, respectively.

Using the velocity $u_N = \beta \Delta T g K/\nu$ as the characteristic velocity scale for natural convection and domain height H as the characteristic length scale, we are able to define the Rayleigh–Darcy number Ra (Rayleigh number for short), expressed as

$$Ra \equiv \frac{u_N H}{\alpha_e} = \frac{H \beta \Delta T g K}{\alpha_e \nu}, \tag{7}$$

where g is the magnitude to the gravitational acceleration rate, K is the permeability. Ra characterizes the macroscopic natural convection. Ra and the traditional Rayleigh number $Ra^* = H^3 \beta \Delta T g/(\alpha \nu)$ has the relationship $Ra = Ra^* Da/\gamma$, where $\gamma = \alpha_e/\alpha$ is the thermal diffusivity ratio. Using the characteristic pore size $K^{1/2}$ as the length scale, we can define the pore-scale Rayleigh number Ra_K, expressed as

$$Ra_K \equiv \frac{u_N K^{1/2}}{\alpha_e} = \frac{\beta \Delta T g K^{3/2}}{\alpha_e \nu}. \tag{8}$$

Ra_K characterizes the pore-scale dispersion due to natural convection. Ra and Ra_K are linked by the Darcy number, expressed as

$$Da \equiv \frac{K}{H^2} = \left(\frac{Ra_K}{Ra}\right)^2. \tag{9}$$

Besides Ra and Ra_K, Gasow et al. show that the convection in porous media is also related to the Prandtl number $Pr = \nu/\alpha$, the viscosity

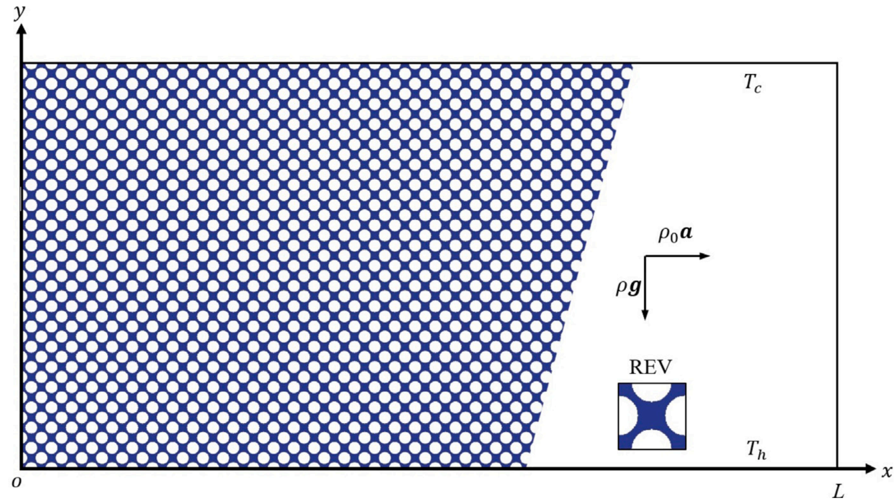

Fig. 1. Computational domain fully occupied by a porous matrix consisting of staggered circular porous elements. The flow is driven by a buoyancy force due to ρg and a horizontal force $\rho_0 \boldsymbol{a}$. The coordinates x_1 and x_2 in the governing equations denote the horizontal x and vertical coordinates y, respectively.

ratio ν_e/ν and the thermal diffusivity ratio $\gamma_m = \alpha_e/\alpha$. Additionally, the acceleration rate a_i results in the forced convection [39]. The characteristic velocity for the forced convection u_F is estimated using the Darcy law $u_F = aK/\nu$. This estimated velocity is found to be very close to the REV-averaged horizontal velocity at the domain center obtained from the DNS results. The pore-scale Peclet number as follows

$$Pe_K \equiv \frac{u_F K^{1/2}}{\alpha_e} = \frac{aK^{3/2}}{\nu \alpha_e}. \tag{10}$$

Pe_K characterizes the forced convection caused by the prescribed horizontal acceleration rate a. The acceleration a is selected to obtain the target values of Pe_K/Ra_K. The macroscopic Eqs. (4)–(6) are not used to calculate the convection in this study but used to analyze the DNS results.

The mixed convection is characterized by the Nusselt number, which is defined as

$$Nu = -\frac{H}{\gamma_m A_w} \int_w \frac{\partial \bar{\theta}}{\partial x_2}\bigg|_w, \tag{11}$$

where w denotes a upper or lower wall surface, while A_w is its area. $^-$ denotes time averaging. $\bar{\theta} = \frac{1}{\Delta t} \int_{t_s}^{t_s+\Delta t} \theta dt$ is the time-averaged dimensionless temperature, where t_s denotes the time at which the convection reaches a statistically steady state. The averaging is performed over the interval Δt, during which the time-averaged quantities remain statistically stationary and the time-averaged Nusselt numbers at the upper and lower walls are identical within numerical accuracy. Note that the thermal diffusivity ratio γ_m is equivalent to the thermal conductivity ratio with the assumption of constant density and specific heat capacity in this study.

2.3. Numerical methods

A finite volume method (FVM) is used for the simulation. The solver is developed based on buoyantBoussinesqPimpleFoam in the open-source code package OpenFOAM 22.12. A second order central difference scheme is used for the spatial discretization. The second order implicit backward scheme is used for time discretization. No under-relaxation is applied in the simulations (relaxation factors equal to 1 for all variables). The convergence tolerances are 10^{-7} for the pressure field and 10^{-12} for both velocity and temperature fields.

The same solver was used in our previous studies [23,39–41]. Differing from the body-fitted meshes used in these studies, we use the staggered mesh to represent the relatively complicated porous matrix geometry in this study. On one hand, this leads to the inaccuracy of the porous element surfaces. On the other hand, we are able to generate the meshes with very high quality (the mesh aspect ratio of 1 and the skewness of 0). It is expected that inaccuracy of the porous element surfaces has negligible effect as the numerical results are mesh-independent. This will be validated in the next section.

3. Studied cases and validation

Mixed convection in a porous medium is affected by many dimensionless parameters. This study focuses on the effects of the Rayleigh number Ra, pore-scale Rayleigh number Ra_K, pore-scale Peclet number Pe_K and porosity ϕ. We calculated 40 DNS cases with $Pe_K/Ra_K = 0$, 0.01, 0.1, 1, $Ra = 1000$, 2000, 5000, 10000, 20000 and $\phi = 0.46$, 0.56. The two-dimensional porous matrix consists of 800 (40 × 20) REVs made of staggered circles shown in Fig. 1. Ra^* can be derived from Ra, γ_m and Da. It is in the range 2.8×10^9–5.7×10^{10} for REV I ($\phi = 0.46$) and 7.3×10^8–1.5×10^{10} for REV II ($\phi = 0.56$).

The Prandtl number, $Pr = \nu/\alpha$, is set to a large value of 250. A large Prandtl number results in relatively small local velocities. Our previous DNS study showed that the local Reynolds number $Re_K = |\mathbf{u}|K^{1/2}/\nu$ for natural convection remains much smaller than unity for $Ra = 20000$ and $Pr = 250$, indicating that the natural convection is well within the Darcy regime [41]. For all cases considered in the present study, the pore-scale Reynolds numbers associated with natural convection, $Re_K^N = u_N K^{1/2}/\nu$, and forced convection, $Re_K^F = u_F K^{1/2}/\nu$, are in the range 0.001–0.056. These values are also significantly smaller than unity, indicating that the convection remains within the Darcy regime.

Additionally, the selected value $Pr = 250$ is within the range encountered in several high-viscosity fluids, including silicone oils and thermal oils, whose Prandtl numbers are often of the order of $10^2 - 10^4$. The governing equations show that Pr is an independent dimensionless parameter. Our previous study demonstrated that, once the Prandtl number is sufficiently large, its influence on the convection becomes relatively weak [40]. Therefore, we expect the present results to remain qualitatively applicable to other high-Prandtl-number fluids. However, for lower Prandtl numbers, the Forchheimer term may no longer be negligible. In such cases, the quantitative behavior may differ from that reported in the present study.

The Darcy number, which characterizes the ratio of the pore scale to the domain scale, is of the order of 10^{-6} in the present study. The Darcy and Rayleigh numbers considered here are comparable to those reported in the experimental study of Keene and Goldstein [42], where the Darcy number is 2.18×10^{-5} and the Rayleigh number reaches 2.03×10^6. Note that the Darcy number of enhanced geothermal reservoirs can be considerably smaller because the characteristic length scale may be

Table 1
Parameters of the DNS cases.

REV	ϕ	Da	K/d^2	γ_m	Ra	Ra_K	Pe_K/Ra_K
I	0.46	1.3×10^{-6}	0.0015	0.27	10^3–2×10^4	1.2–23.0	0–1
II	0.56	3.8×10^{-6}	0.0058	0.36	10^3–2×10^4	2.0–39.2	0–1

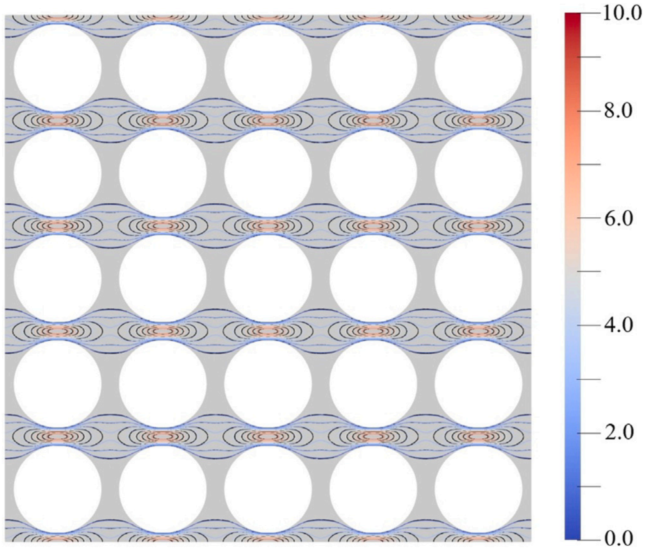

Fig. 2. Contours of dimensionless velocity magnitude $|\boldsymbol{u}|/u_F$ calculated from the staggered mesh (colored) and the body-fitted mesh (black).

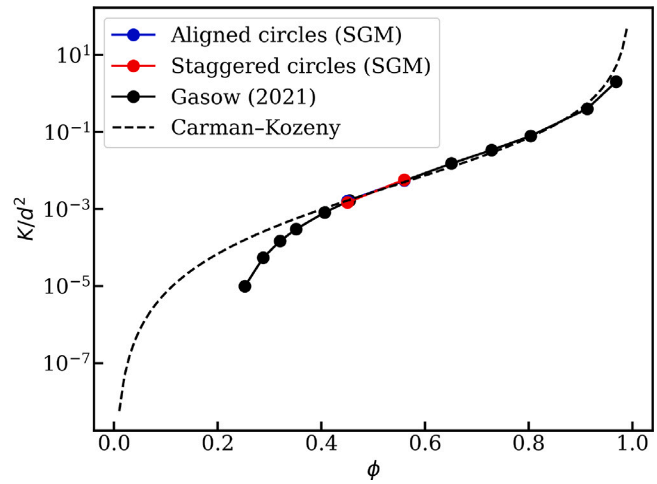

Fig. 3. Dimensionless permeability K/d^2 calculated using a staggered mesh, a body-fitted mesh [39] and the Carman–Kozeny equation [14].

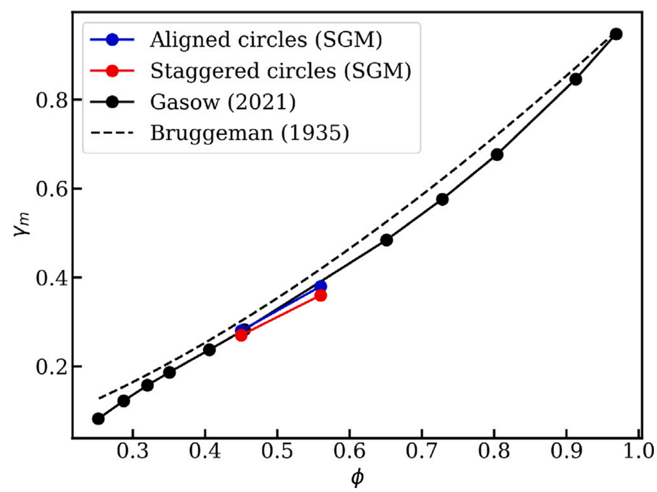

Fig. 4. Thermal diffusivity ratio γ_m calculated using staggered mesh, body-fitted mesh [39] and the Bruggeman correlation [43].

on the order of kilometers while the pore size remains on the order of millimeters. More details about the computational parameters of the studied DNS cases are shown in Table 1.

The numbers of mesh cells used to resolve one REV are N_{REV} = 6600 for REV I and N_{REV} = 8008 for REV II. The ratio of the element diameter to the mesh cell size, d/Δ_c, are 70 for REV I and 64 for REV II. The mesh resolution in this study is higher than in our previous DNS studies, which resolved each REV using 3600 mesh cells (see [23,39,41]). A mesh-sensitivity study shows that the mesh resolution used in this study is sufficient for our analysis, which will be demonstrated below.

Since the DNS solver used in this study has been extensively validated in the previous research, hereby, we will mainly focus on the effect of the staggered mesh on the accuracy of the simulations. First, We simulated the fluid flow driven by a horizontal force $\rho_0 a$ without considering the buoyancy force. The comparison between the staggered mesh (SGM) and body fitted mesh (BFM) approaches is performed using a porous medium composed of aligned circular elements, see Fig. 2. A porous matrix made of staggered circles, which is considered in the main study, is not used in the comparison since it is difficult to generate a high-quality multi-block structured body-fitted mesh for this matrix. As can be seen, the calculated dimensionless velocity contours from the two methods are almost identical.

The permeability of a porous medium, K, can be determined from the numerical results of a pure fluid flow problem shown above. Fig. 3 shows a comparison of the dimensionless permeability, K/d^2, calculated from the present staggered mesh with the results in [39] and the Carman–Kozeny equation [14]. As can be seen, the staggered mesh results are very similar to the references. Additionally, the value of K/d^2 does not change significantly when the circular elements change from aligned to staggered. The Darcy numbers for the cases in this study can be calculated from these permeability values and are shown in Table 1.

The pure heat conduction problem is solved using the porous medium made of aligned circles (shown in Fig. 2) or staggered circles (used in this DNS study) with the upper and lower boundaries at two different temperatures and a periodic boundary condition applied horizontally. The thermal diffusivity ratio γ_m is calculated using the ratio of the heat fluxes with and without the porous matrix. Fig. 4 shows that the staggered mesh results for γ_m of porous media made of aligned circles are in good agreement with the data in [39] and the correlation proposed by Bruggeman [43]. γ_m of a porous medium made of staggered circles is slightly lower than that of a medium made of aligned circles.

The existence of the horizontal flow enhances the heat transfer between the upper and lower boundaries. The thermal diffusion coefficient will increase from α_e to $\alpha_e + \alpha_t$, where α_t is the transverse thermal dispersion coefficient. Fig. 5 shows the dimensionless transverse thermal dispersion coefficients α_t/α_f calculated from the staggered meshes. As can be seen, porous matrices made of staggered circles induce stronger dispersion than those made of aligned circles. However, this

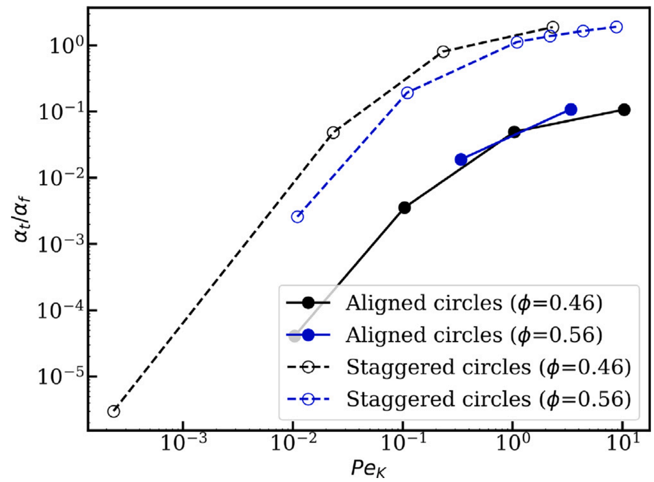

Fig. 5. Ratio of the transverse thermal dispersion coefficient to the diffusion coefficient α_t/α_f, calculated using the staggered mesh.

is only important at high Peclet numbers. The longitudinal thermal dispersion coefficient α_l is usually much larger α_t, however, it is difficult to determine its value. Instead of evaluating the longitudinal dispersion coefficients, we will discuss the effect of dispersion on mixed convection directly based on our DNS results.

The DNS cases of pure natural convection in a porous medium made of aligned circles in [23] are calculated again using the present staggered mesh with different resolutions (N_{REV} = 2920, 6540 and 11628), see Fig. 6a. The calculated Nusselt numbers decrease slightly as the mesh resolution increases from N_{REV} = 2920 to 6540 and minimally as N_{REV} is further increased to 11628. Based on this study, the mesh resolutions used in the present work are N_{REV} = 6600 for REV I and N_{REV} = 8008 for REV II. The mesh sensitivity study for staggered circular elements shown in Fig. 6b confirm that these mesh resolutions are sufficient for the analysis. The corresponding total numbers of mesh cells are approximately 5.3 million for REV I and 6.4 million for REV II. The SGM result of Nu at Ra = 20000 is about 7% higher than the DNS results in [23]. This discrepancy is partly due to the inaccuracy of the circular element surfaces in the SGM. Conversely, the body-fitted meshes employed in [41] exhibit greater skewness and aspect ratios. This leads to larger numerical dissipation and reduces the Nusselt number. These factors may contribute to differences in numerical accuracy and therefore provide an indication of the uncertainty associated with the simulations.

4. Results and discussion

This study focuses on the effects of horizontal flow on Nusselt numbers, plume structures, flow and temperature statistics, and temperature transport. These topics will be discussed in the following subsections.

4.1. Nusselt number

As global results, the Nusselt numbers for all 40 DNS cases are shown in Fig. 7. Similar to the natural convection in a porous medium composed of aligned circles [23,39,41], the Nusselt number for staggered circles also decreases as the porosity ϕ increases. A possible reason is that larger porosity results in stronger dispersion, which weakens the flow instability and thus reduces the Nusselt number. However, the vertical dispersion also enhances the heat transfer. Additionally, Gasow et al. report that an increase in the porosity leads to a higher macroscopic diffusion coefficient [39]. This means that the Nusselt number can still decrease as the porosity ϕ increases even if the dispersion has a negligible effect. The Nusselt number for pure natural convection follows the scaling law $Nu \sim Ra^a$ with a = 0.5, which is in agreement with [24] and close to the experiment by Keene and Goldstein, who found the scaling law of $Nu \sim Ra^{0.319}$ [42].

The DNS results show that the horizontal flow has an apparent effect on the Nusselt number when $Pe_K/Ra_K \geq 0.1$. This appears to be different from the experimental study by Michel-Meyer et al. who suggest that the constant dissolution flux for solutal convection (convection driven by mass transfer) is not affected by horizontal flows [33]. It is also different from the numerical study by Tsinober et al. who suggest that the horizontal flow starts to affect solutal convection as $Pe/Ra \geq 0.77$ (Pe/Ra is equivalent to Pe_K/Ra_K). This discrepancy is due to the fact that solutal convection in porous media usually occurs at very low Ra_K (typically 10^{-3} [40]), while Ra_K for thermal convection is often much larger due to larger sizes of porous elements. Ra_K in this study ranges from 1.2 to 39.2, for which the pore-scale dispersion is significant. The horizontal flow is expected to weaken the small-scale fluctuations due to both macroscopic advection and pore-scale dispersion, thus reducing the Nusselt number. Fig. 7 shows that the Nusselt number decreases more significantly with Pe_K/Ra_K as Ra increases, at which the dispersion is stronger. The scaling coefficient a decreases with increasing Pe_K/Ra_K and Ra. At a fixed Pe_K/Ra_K value, the scaling coefficient a of the present cases can be approximated as $a = 0.5 - 2.5 \times 10^{-6} Pe$, where $Pe = RaPe_K/Ra_K = u_F K^{1/2}/H$ is the macroscopic Peclet number. This means that, although the convection is significantly affected by the pore-scale dispersion, the effect of the horizontal flow can be approximated using the macroscopic Peclet number Pr. Note that the current correlation is intended to predict the trend of how Nu varies with Ra, rather than to provide highly accurate predictions of the Nusselt number for mixed convection under all conditions. Developing a more general correlation capable of accurately predicting Nu would require a more comprehensive study and a substantially larger dataset.

4.2. Plume structures

Transient natural convection in a porous medium is characterized by mega-plumes in the interior region and proto-plumes near the boundaries [41]. These small proto-plumes are the result of the instabilities growing in the boundary layers, which cause high-temperature fluid to rise and low-temperature fluid to sink. Due to fluctuations in horizontal flows, these proto-plumes merge to generate large mega-plumes. In realistic natural convection, where pore-scale effects cannot be neglected, the plumes are affected not only by molecular diffusion and macroscopic advection but also by pore-scale dispersion, complicating plume dynamics.

Our previous DNS study [41] showed that, at a fixed Rayleigh number, increasing the pore size enhances pore-scale dispersion and reduces the number of mega-plumes. Likewise, for a fixed porous structure, increasing the Rayleigh number through a higher characteristic velocity also strengthens dispersion, resulting in fewer mega-plumes than predicted by DOB simulations, where dispersion effects are neglected.

The number of mega-plumes in the present DNS results is very stable and can be counted unambiguously from the snapshots. The results of natural convection are consistent with the mechanism obtained in our previous study. As seen in Fig. 8a, only two mega-plumes are found in the interior region at Ra = 20000 with a corresponding wavenumber of $k = \pi L/l_p = 2\pi$, where l_p is the mean spacing between two mega-plumes. This is much lower than the wavenumber calculated from a DOB simulation $k = 9\pi$, where the pore-scale dispersion is neglected [19]. This value is also lower than the wavenumber for the natural convection in a porous medium made of aligned circles $k = 4\pi$ [41], which has weaker pore-scale dispersion. By contrast, at a lower Rayleigh number (Ra = 1000), three mega-plumes are observed in the interior region, see Fig. 9a.

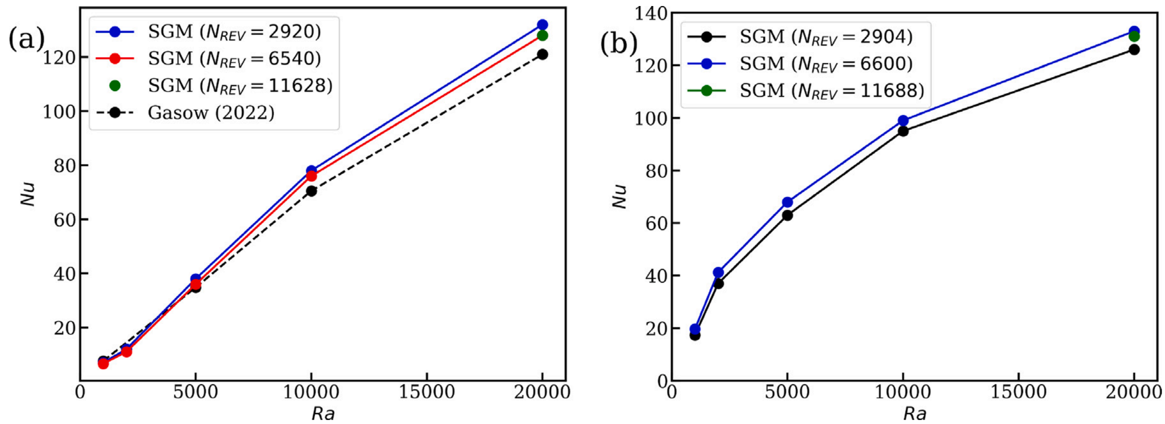

Fig. 6. Nusselt number for natural convection in a porous medium composed of (a) aligned circular elements (ϕ = 0.45) and (b) staggered circular elements (ϕ = 0.46). The DNS results for the aligned circular elements are compared with those of Gasow et al. [23]. Both porous matrices consist of 800 REVs (40 × 20) with the Rayleigh number ranges from 1000 to 20000.

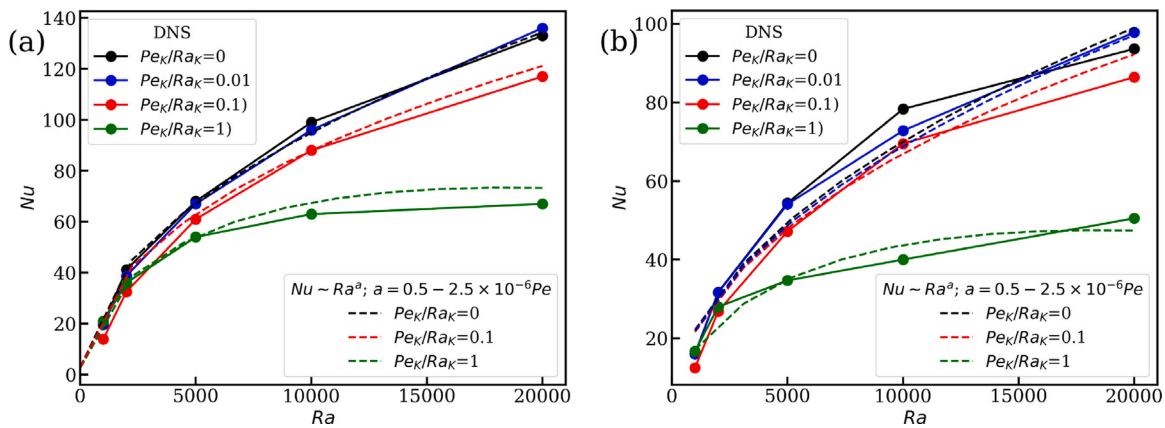

Fig. 7. Nusselt number, Nu, as a function of Rayleigh number, Ra, for natural convection ($Pe_K/Ra_K = 0$) and mixed convection ($Pe_K/Ra_K > 0$) in porous media composed of staggered circular elements with ϕ = 0.46 (a) and ϕ = 0.56 (b). The DNS results are compared with the scaling relationship $Nu \sim Ra^a$ with $a = 0.5 - 2.5 \times 10^{-6} Pe$.

The imposed horizontal flow introduces additional dispersion into the system. For the present cases ($Pe_K/Ra_K \leq 1$), its influence on the buoyancy-driven convection is more important than the direct contribution of the additional dispersion itself. The extra dispersion caused by the horizontal flow smooths the small-scale temperature and velocity fluctuations within the thermal boundary layer and weakens the lateral interactions between neighboring proto-plumes, and thus makes the temperature more uniformly distributed in the boundary layer. Its effect is similar as enhancing diffusive transport and reducing the effective Rayleigh number. As a result, proto-plume merging becomes less frequent, allowing more proto-plumes to survive and develop into individual mega-plumes.

The snapshots from the DNS results confirm this, showing that the number of mega-plumes increases from two to four at Ra = 20000 as Pe_K/Ra_K increases from 0 to 0.1 (Fig. 8b), and from three to four at Ra = 1000 (Fig. 9b). The number of mega-plumes increases to five at Ra = 1000 when Pe_K/Ra_K is increased to 1 (Fig. 9c). However, the macroscopic instability due to transient advection seems considerably weakened at Ra = 20000 as Pe_K/Ra_K is increased to 1. Only one large mega-plume is found in the snapshot (Fig. 8c). Although the remaining mega-plume at $Pe_K/Ra_K = 1$ occupies a larger spatial region, it is mainly associated with the reduction of the proto-plumes (and increasing spacing). Consequently, the thermal boundary layer becomes substantially thicker. This indicates a weaker convective transport contribution and a relatively larger role of conduction within the thermal boundary layer.

Fig. 10 shows the wavenumbers of the mega-plumes for all DNS cases. These results are compared to the correlation $k = 0.48Ra^{0.4}$ proposed by Hewitt et al. based on the DOB simulations [21]. The calculated wavenumbers for pure natural convection only resemble the correlation results at Ra = 1000, when pore-scale dispersion is weak. Wavenumbers at higher Rayleigh numbers are all lower than the correlation results. At Ra = 1000, the wavenumber increases as Pe_K/Ra_K increases. Conversely, at high Rayleigh numbers (Ra = 10000 or 20000), the wavenumber reaches its maximum value at Pe_K/Ra_K = 0.1. The DNS results show that horizontal flow has a significant effect on the plume structures.

4.3. Velocity and temperature statistics

We analyze the velocity and temperature statistics to better understand the plume dynamics. First, we take a time average of the flow and temperature fields to obtain the time-averaged temperature, $\bar{\theta}$, the r.m.s. temperature, θ', and the r.m.s. velocity components u' and v'. Then, we perform volume averaging on these fields across the fluid portion of each REV. We define the macroscopic coordinates with the center of the fluid portion of an REV, denoted as $\hat{x}$ and $\hat{y}$. Note that the REV is cut by the boundary surface when $\hat{y} < s/2$, where s is the REV size. Finally, we perform horizontal-line averaging of the REV-averaged fields. These results are denoted as $\hat{\theta}$, $\hat{\theta}'$, $\hat{u}'$ and $\hat{v}'$, which depend on $\hat{y}$.

Fig. 11 shows the distribution of the mean temperature function $\left(1 - \hat{\theta}\right) Ra^{-0.5}$ in the wall normal direction. As can be seen, the diffusive

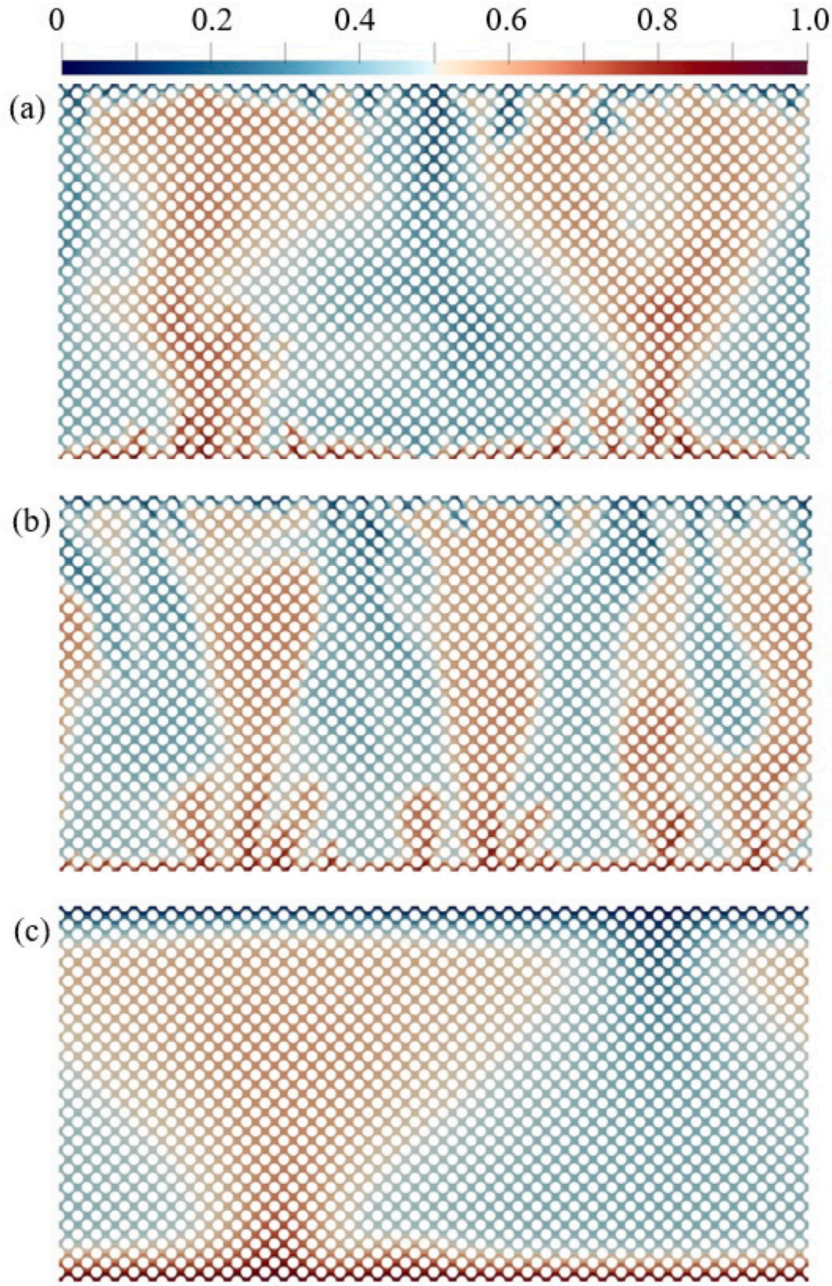

Fig. 8. Snapshots of the instantaneous temperature (θ) fields at $Ra = 20000$ and $Pe_K/Ra_K = 0$ (a), 0.1 (b) and 1 (c).

layer, in which the molecular diffusion dominates the heat transfer, is only about 1/10 the size of a REV. This layer is characterized by a linear relationship between the dimensionless temperature and the dimensionless wall normal displacement. Horizontal flow does not significantly affect the boundary layer thickness. The scaling law of $\left(1-\hat{\theta}\right) Ra^{-0.5} \sim \hat{y}/s$ can be found in the diffusive layer as $5000 \le Ra \le 20000$. This indicates that the Nusselt number follows the scaling law $Nu \sim Ra^{0.5}$ within this range of Rayleigh numbers. This is smaller than the scaling coefficient 0.8 obtained in [41] since the porous matrix made of staggered circles in this study induces stronger dispersion. This is similar to the thermal convection experiment by Keene and Goldstein, who found the scaling law of $Nu \sim Ra^{0.319}$ [42]. This scaling law remains valid as Pe_K/Ra_K increases to 0.1, see Fig. 11b. However, the scaling coefficient becomes slightly larger than 0.5 as $1000 \le Ra \le 5000$ due to the weaker dispersion at lower Rayleigh numbers.

Figs. 12 and 13 show the distribution of the temperature and velocity statistics $\hat{\theta}$, $\hat{\theta}'$, $\hat{u}'/u_N$ and $\hat{v}'/u_N$ in the wall-normal direction. At $Ra = 20000$, the mean temperature, $\hat{\theta}$, increases as Pe_K/Ra_K increases in the boundary layer (Fig. 12a). This is because the introduced horizontal flow enhances the mixing of fluid with different temperatures, while weakening vertical advection, which agrees with the Nusselt number trend shown in Fig. 7a. At $Ra = 1000$, the mean temperature $\hat{\theta}$ changes very slightly in the boundary layer as Pe_K/Ra_K increases from 0 to 0.1. However, it increases significantly as Pe_K/Ra_K increases to 1, which suggests enhanced mixing in the boundary layer.

As Pe_K/Ra_K increases from 0 to 0.1, the temperature and velocity fluctuations become larger in the interior region. These results are in agreement with the trend of mega-plume numbers shown in Figs. 8 and 9, which increase Pe_K/Ra_K increases from 0 to 0.1. However, the fluctuations of pure natural convection and mixed convection cannot be directly compared, as the former is solely due to flow instabilities and the latter is due to both flow instabilities and the transport of the plumes in the horizontal direction. It is expected that transporting the

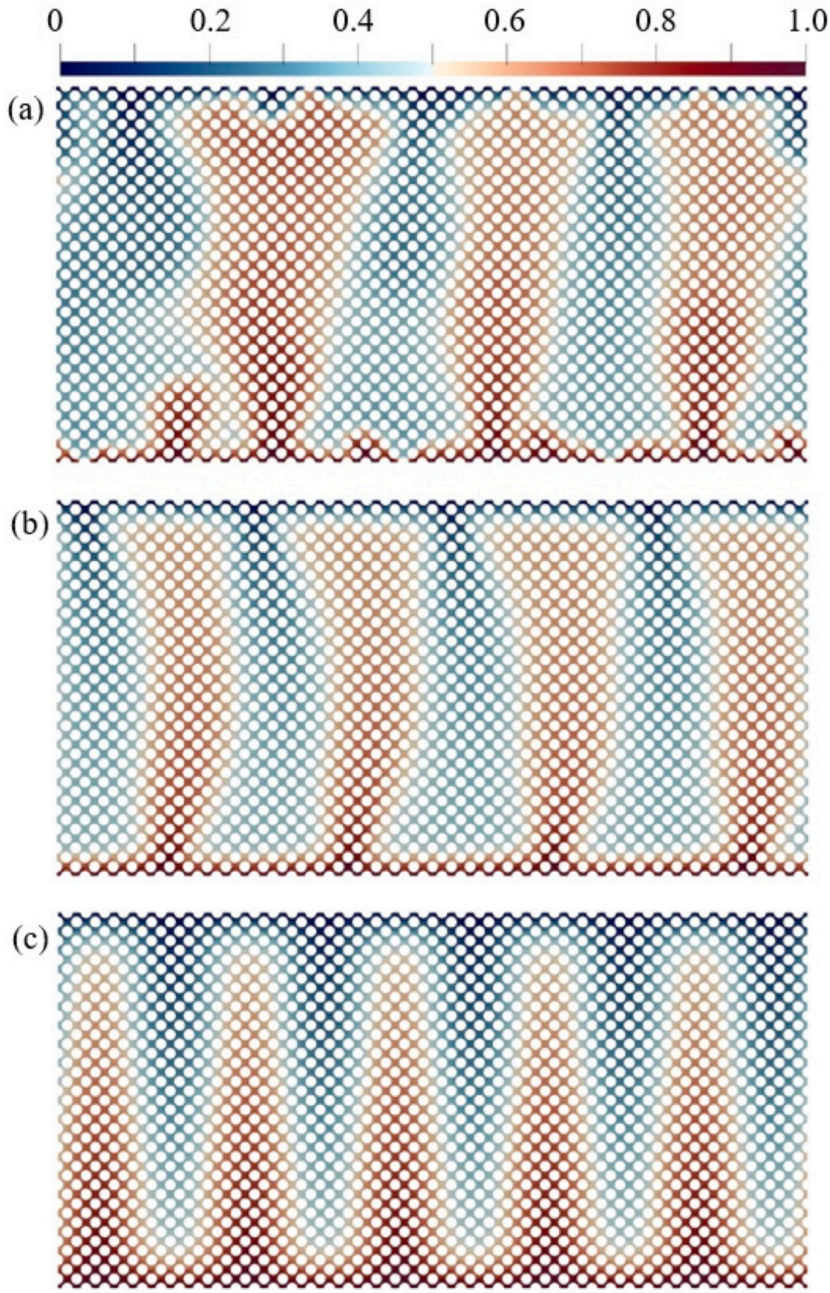

Fig. 9. Snapshots of the instantaneous temperature (θ) fields at $Ra = 1000$ and $Pe_K/Ra_K = 0$ (a), 0.1 (b) and 1 (c).

mega-plumes at a constant velocity will not affect the flow structures near the wall, so that it would have a minimal impact on the heat transfer. As a result, the Nusselt number does not increase as Pe_K/Ra_K increases from 0 to 0.1. As Pe_K/Ra_K increases from 0.1 to 1, the fluctuations in the interior region decrease at $Ra = 20000$, see Fig. 12b, c and d, and increase at $Ra = 1000$. These results are in agreement with the trend of mega-plume numbers and Nusselt numbers.

At a lower Rayleigh number of $Ra = 1000$, the temperature fluctuation $\hat{\theta}'$ in the boundary layer becomes weaker as Pe_K/Ra_K increases. Meanwhile the velocity fluctuations $\hat{u}'$ and $\hat{v}'$ do not change significantly (Fig. 13). This indicates that the horizontal flow weakens the flow instability near the wall. The effect of the horizontal flow in the boundary layer is more complicated at a large Rayleigh number $Ra =$ 20000. As can be seen, fluctuations of both temperature and velocity are the strongest at $Pe_K/Ra_K = 0.1$. However, Fig. 7 shows that the Nusselt number does not increase as Pe_K/Ra_K increases from 0 to 0.1. This is still because stronger fluctuations do not necessarily indicate stronger flow instabilities. In mixed convection, the fluctuations are also caused by the transport of the plumes in the horizontal directions which does not significantly affect the heat transfer at the wall.

Fig. 14 compares the statistical results for different porosity (ϕ) values. The mean temperature $\hat{\theta}$ does not change significantly as ϕ increases from 0.46 to 0.56. Considering Nu is inversely proportional to γ_m and γ_m increases with ϕ, it can be found that Nu increases with a decrease in ϕ. This is in consistent with the DNS results for Nu shown in Fig. 7. Fig. 14 also shows that the temperature and velocity

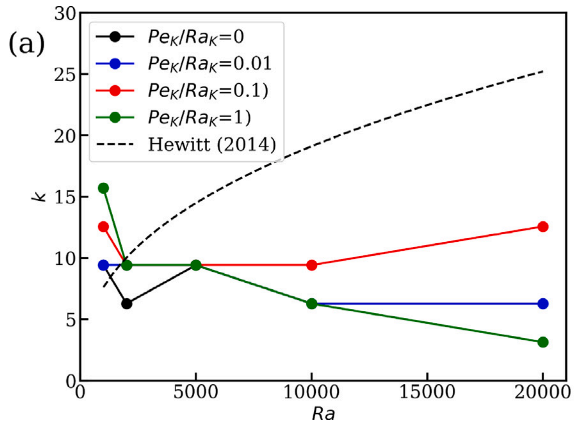

Fig. 10. Wavenumber k as a function of Rayleigh number Ra for natural convection ($Pe_K/Ra_K = 0$) and mixed convection ($Pe_K/Ra_K > 0$) in porous media composed of staggered circular elements with $\phi = 0.46$ (a) and $\phi = 0.56$ (b). The DNS results are compared with the correlation $k = 0.48Ra^{0.4}$ proposed by Hewitt et al. [21].

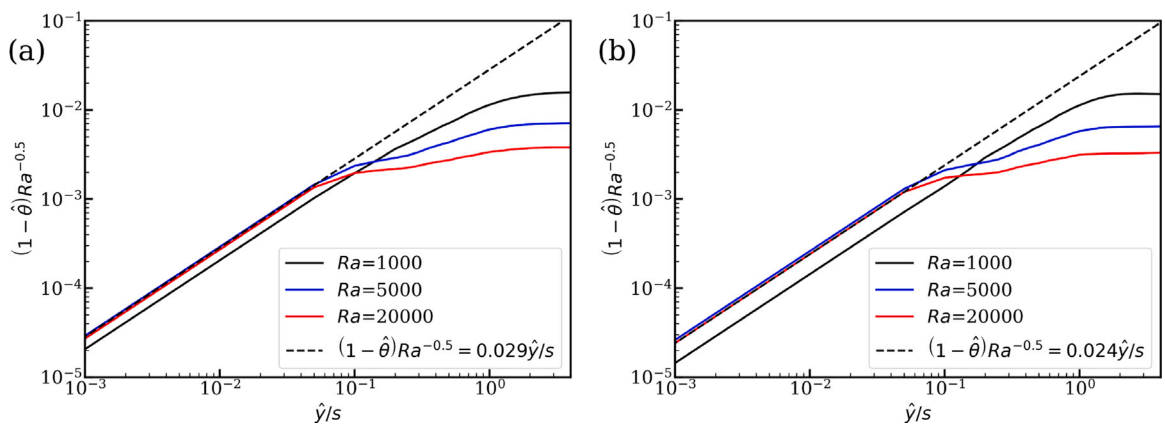

Fig. 11. Profiles of the scaled mean dimensionless temperature, $(1-\hat{\theta})Ra^{-0.5}$, plotted versus $\hat{y}/s$ within the first four REVs adjacent to the lower boundary for $Pe_K/Ra_K = 0$ (a) and $Pe_K/Ra_K = 0.1$ (b).

fluctuations become weaker as ϕ increases, this is also consistent with the Nusselt number trend, which decreases as the porosity increases. The DNS results for other Rayleigh numbers are not shown here.

4.4. Transport of temperature

The DNS results of the transient flow and temperature fields are averaged in the fluid portion of each REV to obtain the instantaneous macroscopic fields. From these macroscopic fields, we can calculate the dimensionless macroscopic advection vector component Φ_i, the pore-scale dispersion vector component Ψ_i, and the molecular diffusion vector, which are defined as

$$\Phi_i = \left(\langle u_i\rangle^i - u_F\delta_{i,1}/\phi\right)\langle\theta\rangle^i/u_N, \tag{12}$$

$$\Psi_i = \left\langle {}^iu_i\,{}^i\theta\right\rangle^i/u_N = \left(\langle u_i\theta\rangle^i - \langle u_i\rangle^i\langle\theta\rangle^i\right)/u_N, \tag{13}$$

$$\Gamma_i = -\frac{\alpha_e}{\phi u_N}\frac{\partial\langle\theta\rangle^i}{\partial\hat{x}_i}. \tag{14}$$

$u_F\delta_{i,1}/\phi$, which is the velocity caused by the horizontal acceleration rate a_i, is extracted from $\langle u_i\rangle^i$ in Eq. (12) since it is uniform in the medium and does not affect the heat transfer directly. Eq. (6) suggests that the transport of temperature is determined by these three vectors. If we take a line and time averaging of Eq. (6), integrating the equation from 0 to x_2, and consider the definition of the Nusselt number, we can obtain

$$Nu = \phi Ra\left\langle\bar{\Phi}_2 + \bar{\Psi}_2 + \bar{\Gamma}_2\right\rangle_x, \tag{15}$$

where $\langle\bar{\Phi}_2\rangle_x$, $\langle\bar{\Psi}_2\rangle_x$ and $\langle\bar{\Gamma}_2\rangle_x$ are the averaged advection, dispersion and diffusion in the horizontal (x-) direction, respectively.

Figs. 15 and 16 show typical snapshots of the advection and dispersion components in the horizontal direction (Φ_1 and Ψ_1) and in the vertical direction (Φ_2 and Ψ_2) at $Ra = 1000$. As can be seen, the dispersion is about an order of magnitude lower than the advection. Generally, the values of dispersion are larger in the boundary layers than in the interior region. However, some streaks of larger Ψ_2 values can still be observed in the interior region (Figs. 16c and d). Their locations are close to the interfaces of $\Phi_2 = 0$.

The pore-scale dispersion has two competing effects on the vertical heat transfer. For pure natural convection, when the Rayleigh number is kept constant, increasing the pore size strengthens the pore-scale dispersion. On the one hand, the stronger dispersion promotes the mixing of fluid parcels and enhances the vertical transport of heat. On the other hand, it enhances the merging of proto-plumes, reducing the number of mega-plumes. Consequently, pore-scale dispersion can either enhance or weaken the overall heat transfer, depending on the relative importance of these two effects. This effect was shown in our previous study [41], indicating that increasing the pore-size does not have to reduce the Nusselt number.

The imposed horizontal flow introduces additional dispersion into the system. However, for the present cases ($Pe_K/Ra_K \le 1$), its influence on the buoyancy-driven convection is mainly more important than the direct contribution of the additional dispersion itself. The horizontal flow smooths the small-scale temperature and velocity fluctuations within the thermal boundary layer and weakens the lateral interactions

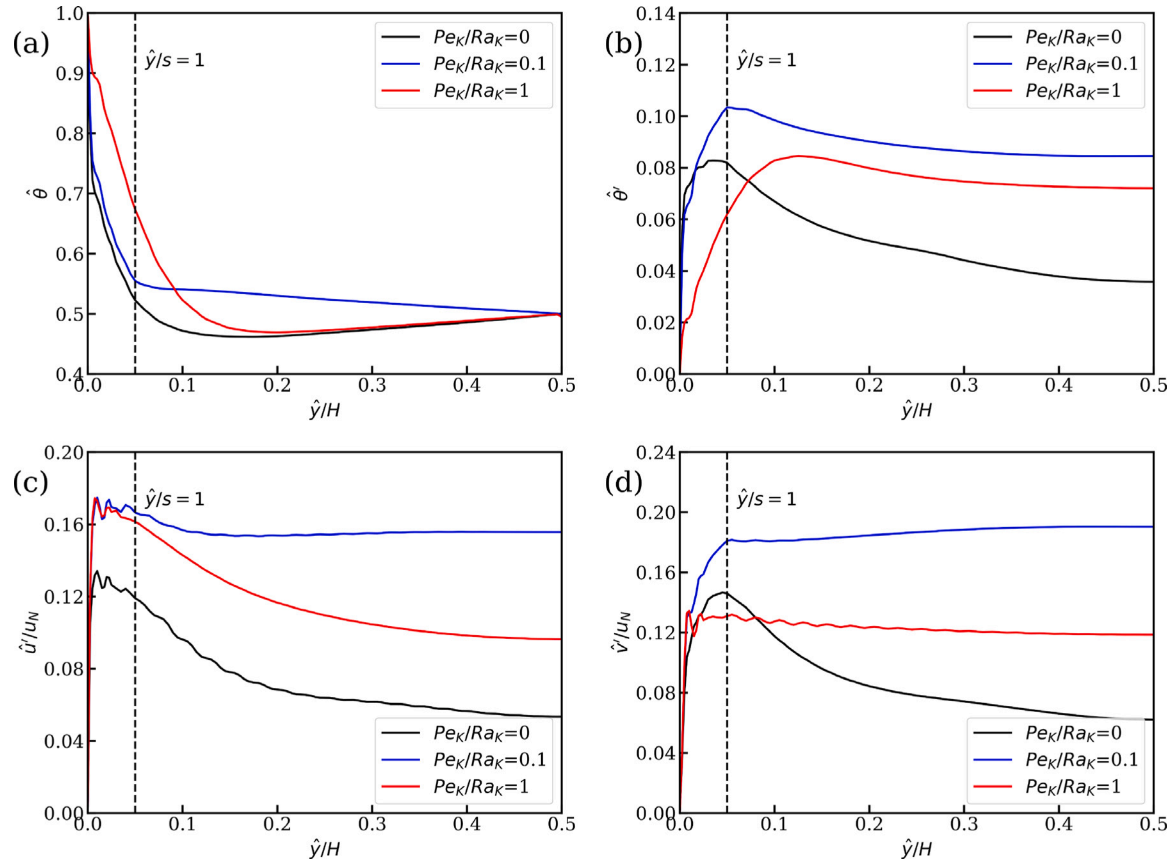

Fig. 12. Wall-normal profiles of the dimensionless mean temperature, $\hat{\theta}$ (a), r.m.s. temperature, $\hat{\theta}'$ (b), and r.m.s. velocity fluctuations, $\hat{u}'/u_N$ (c) and $\hat{v}'/u_N$ (d), plotted versus $\hat{y}/s$ for $Ra = 20000$. Results are shown for Pe_K/Ra_K ranging from 0 to 1.

between neighboring proto-plumes. From a macroscopic perspective, this effect resembles an increase in diffusive transport and reduces the intensity of the plume dynamics near the walls. This is confirmed in the DNS results, which show that the irregular fluctuation of Φ_1 near the boundary layer for pure natural convection (Fig. 15a) becomes more regular and weaker (Fig. 15b) as Pe_K/Ra_K increases. Ψ_1 has a similar trend (see Figs. 15c and d for comparison). The weakened plume merging allows more proto-plumes to survive and develop into individual mega-plumes. Consequently, the number of mega-plumes increases from three to four as Pe_K/Ra_K increases from 0 to 0.1. This provides additional pathways for heat transfer, thereby enhancing heat transfer and increasing the Nusselt number, which is called an "enhancing" effect.

On the other hand, the reduced buoyancy-driven fluctuations weaken the vertical exchange between the wall region and the core region, thereby reducing the vertical advection and pore-scale mechanical dispersion. The DNS results provide clear evidence of this mechanism. For pure natural convection, the snapshots of Φ_2 (Fig. 16a) and Ψ_2 (Fig. 16c) reveal numerous small-scale plume structures associated with vertical advection and dispersion. These structures promote the transport of heat from the lower wall toward the upper wall and therefore contribute to the overall heat transfer. As Pe_K/Ra_K increases to 0.1, these small-scale structures are substantially weakened. The effect is similar to an increase in diffusive transport. Consequently, the vertical transport is reduced, leading to a lower Nusselt number. This mechanism is referred to as the "weakening" effect. Since the "weakening" effect dominates over the competing enhancement effect in this regime, the Nusselt number decreases as Pe_K/Ra_K increases from 0 to 0.1.

Fig. 17 shows the distribution of the horizontal line- and time-averaged total advection component ($\langle \bar{\Phi}_2 + \bar{\Psi}_2 \rangle_x$), which makes the effect of the horizontal flow on the transport of temperature more clearly observable. At $Ra = 1000$, $\phi Ra \langle \bar{\Phi}_2 + \bar{\Psi}_2 \rangle_x$ approaches the Nusselt number shown in Fig. 7a in the region two REVs away from the wall ($\hat{y} \geq 2s$), where advection dominates. This indicates that molecular diffusion is only important in the region within approximately two REVs from the wall. As Pe_K/Ra_K increases from 0 to 0.1, it can be clearly seen that $\langle \bar{\Phi}_2 + \bar{\Psi}_2 \rangle_x$ becomes smaller, suggesting weaker convection. Convection is enhanced as Pe_K/Ra_K increases from 0.1 to 1 since the surviving mega-plumes have a more important effect. Fig. 18a shows the distribution of the horizontal-line-averaged macroscopic advection component, $\langle \Phi_2 \rangle_x$, and the pore-scale dispersion component, $\langle \Psi_2 \rangle_x$. There are still perturbations in the interior region since the results are not time-averaged due to the computational cost. However, it can be seen that the dispersion mainly takes place in the first REV next to the wall. Both $\langle \Phi_2 \rangle_x$ and $\langle \Psi_2 \rangle_x$ decrease as Pe_K/Ra_K increases from 0 to 0.1, and increase as Pe_K/Ra_K increases from 0.1 to 1.

A similar phenomenon can be observed at a higher Rayleigh number ($Ra = 20000$, $Ra_K = 23$). Figs. 19a and 20a show that the plumes merge strongly in the boundary layers for pure natural convection, while only two mega-plumes survive in the interior region. The imposed horizontal flow weakens the pore-scale dispersion. Consequently, more plumes appear in the boundary layers. Fig. 20b shows approximately nine plumes in the lower boundary layers. The corresponding wavenumber is 8π, which is close to $k \approx 25$ according to the correlation $k = 0.48Ra^{0.4}$ proposed by Hewitt, et al. [21]. However, most of these plumes cannot evolve into mega-plumes because the remaining pore-scale dispersion is still strong. Instead, these small plumes generate additional vertical pore-scale dispersion around their boundaries, thereby enhancing the heat transfer. Fig. 20d indicates this effect, showing that some plumes with high values of Ψ_2 extend to the interior region. Fig. 18b also shows that the vertical dispersion component, $\langle \Psi_2 \rangle_x$, increases in the interior region as Pe_K/Ra_K increases from 0 to 0.1.

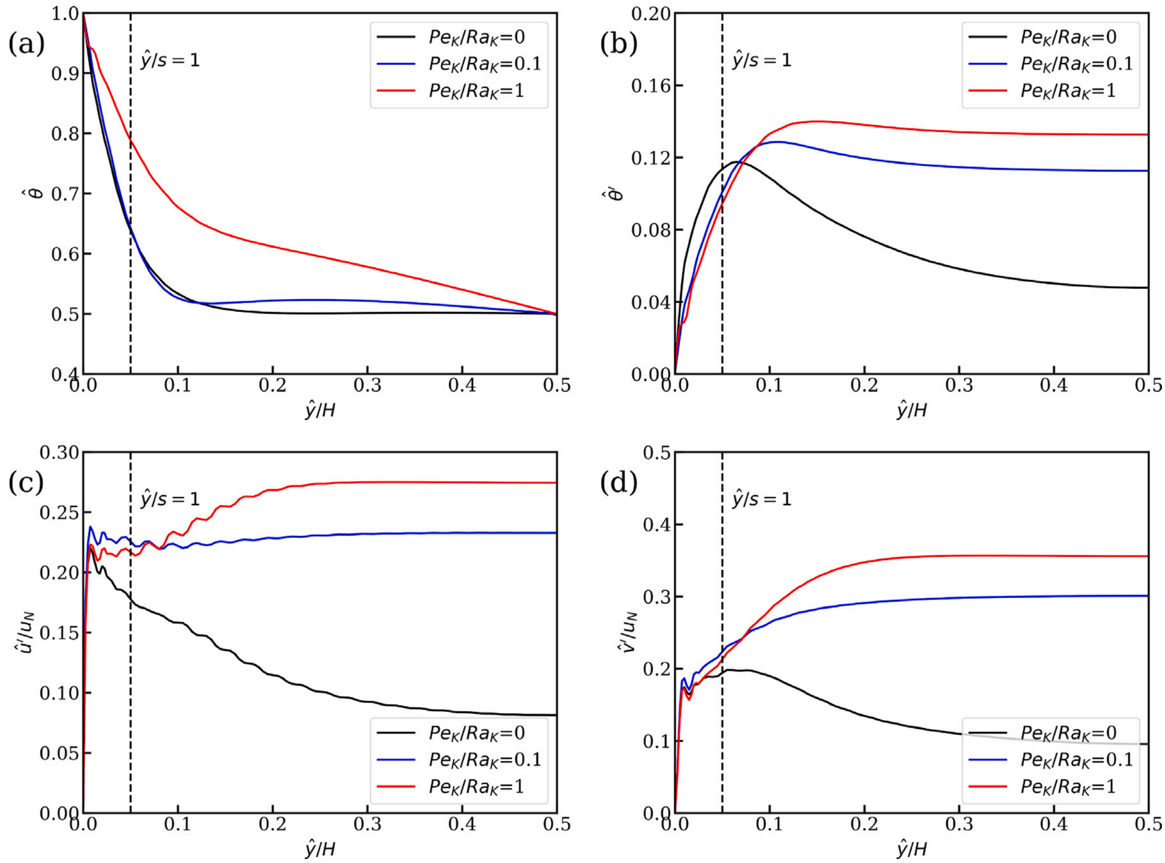

Fig. 13. Wall-normal profiles of the dimensionless mean temperature, $\hat{\theta}$ (a), r.m.s. temperature, $\hat{\theta}'$ (b), and r.m.s. velocity fluctuations, $\hat{u}'/u_N$ (c) and $\hat{v}'/u_N$ (d), plotted versus $\hat{y}/s$ for $Ra = 1000$. Results are shown for Pe_K/Ra_K ranging from 0 to 1.

As the horizontal flow prevents the larger plumes from merging and enhances convection to some extent, it also weakens small-scale fluctuations, thereby reducing the Nusselt number. As a result of these competing effects, the total vertical advection ($\langle \bar{\Phi}_2 + \bar{\Psi}_2 \rangle_x$) as well as the Nusselt number decrease slightly as Pe_K/Ra_K increases from 0 to 0.1, see Fig. 17b.

In addition to weakening the dispersion caused by natural convection, the horizontal flow itself causes extra horizontal dispersion. This enhances the merging of the plumes and reduces the Nusselt number. The "weakening" effect of the dispersion caused by the horizontal flow becomes dominant at large Rayleigh and Peclet numbers ($Pe_K/Ra_K = 1$, $Ra = 20000$). In this case, only one mega-plume is found, and the flow and temperature fields become almost steady (Fig. 8c). Correspondingly, the vertical advection and dispersion also decrease significantly (Fig. 18b).

The DNS results above demonstrate the significant effect of the pore-scale dispersion on heat transfer. It is traditionally modeled using a Fickian dispersion tensor, $D_{ij} = (\alpha_l - \alpha_t)\,|\mathbf{u}_D|\,n_i n_j + \alpha_t\,|\mathbf{u}_D|\,\delta_{ij}$ and $\phi\left\langle {}^i u_i^i \theta \right\rangle^i = D_{ij}\partial\langle T\rangle^i/\partial x_j$, where n_i and n_j are the components of the unit velocity vector. α_l and α_t are the longitudinal and transverse dispersivities, respectively. $\mathbf{u}_D$ is the superficial velocity vector. The DNS show that the dispersion process is inherently anisotropic and that both the magnitude and anisotropy of the effective dispersion tensor depend on the relative strengths of natural and forced convection. Therefore, an isotropic dispersion model with constant coefficients would not accurately represent the dispersion term under mixed-convection conditions.

The DNS results also show that the dispersion patterns are significantly affected by the imposed horizontal flow. It is still not clear whether traditional dispersion models remain valid for mixed convection. Assessing the accuracy of such models would require extensive macroscopic simulations employing established dispersion closures, followed by direct comparisons with the DNS results. In addition, a reliable quantitative determination and parameterization of the effective longitudinal and transverse dispersivities would require a dedicated closure analysis and DNS data covering a broader range of parameters. The current dataset is still not sufficient to determine whether these coefficients can be treated as constants, how they depend on the local flow state, or whether a Fickian dispersion model remains adequate under mixed-convection conditions. This will be our future work.

5. Conclusions

A DNS study is performed to better understand the mixed convection in a porous medium chamber bounded by two walls. Natural convection is caused by density variations in the chamber, which are driven by the temperature difference between the two walls. An acceleration force is prescribed in the horizontal direction to cause the forced convection. The convection for $1000 \le Ra \le 20000$, $1.2 \le Ra_K \le 39.2$, $0 \le Pe_K/Ra_K \le 1$, the Prandtl number $Pr = 250$, and $\phi = 0.46$ and 0.56 is studied based on the DNS results.

Pore-scale dispersion plays an important role in the convection due to the relatively high Ra_K in this study. Dispersion enhances the merging of the small plumes in the boundary region. The plume wavenumbers of the studied cases only approach to the correlation $0.48Ra^{0.4}$ at the smallest Rayleigh number $Ra = 1000$, where the dispersion is the weakest. The wavenumbers for all the other cases are larger than the correlation results.

The extra dispersion caused by the horizontal flow smooths the small-scale temperature and velocity fluctuations within the thermal boundary layer. As a result, proto-plume merging becomes less frequent, allowing more proto-plumes to survive and develop into individual mega-plumes. At $Ra = 1000$, the plume number increases from

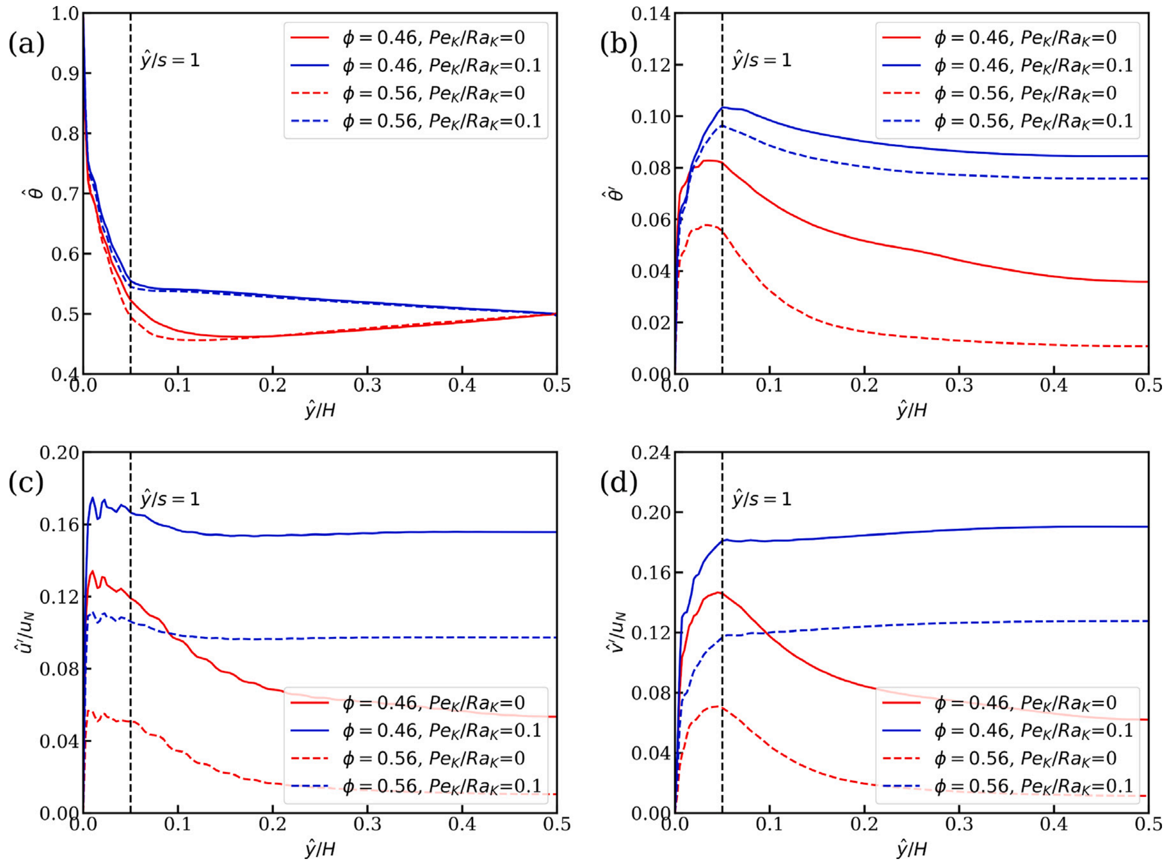

Fig. 14. Wall-normal profiles of the dimensionless mean temperature, $\hat{\theta}$ (a), r.m.s. temperature, $\hat{\theta}'$ (b), and r.m.s. velocity fluctuations, $\hat{u}'/u_N$ (c) and $\hat{v}'/u_N$ (d), plotted versus $\hat{y}/s$ for $Ra = 20000$. Results are compared for $Pe_K/Ra_K = 0$ and 0.1, and for porosities $\phi = 0.46$ and 0.56.

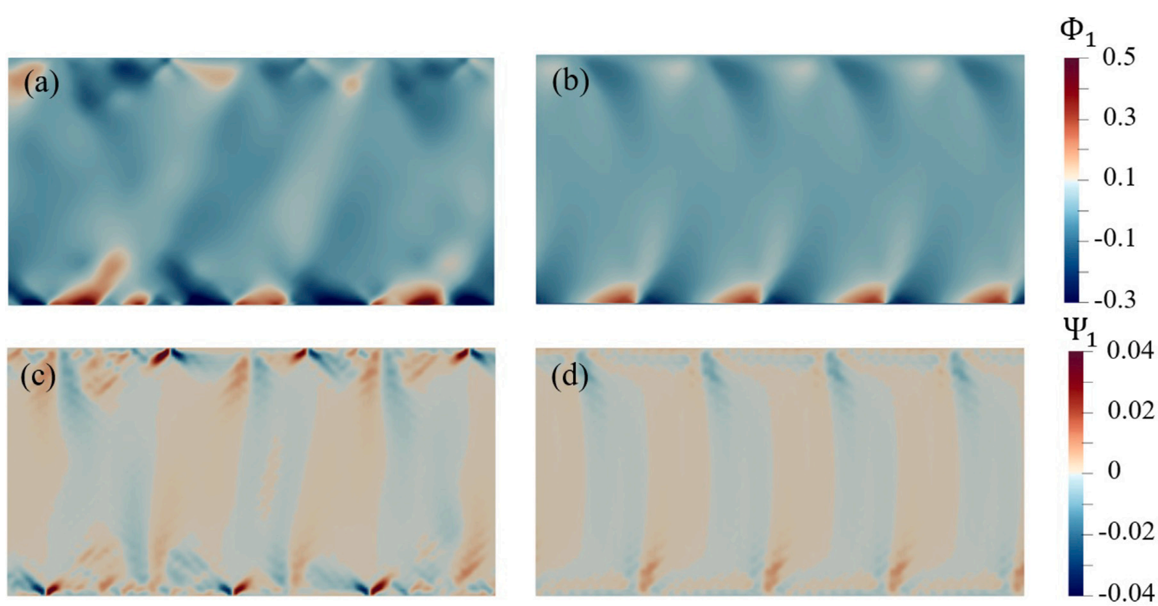

Fig. 15. Snapshots of the horizontal macroscopic advection, Φ_1 (a,b), and horizontal pore-scale dispersion, Ψ_1 (c,d), at $Ra = 1000$, comparing $Pe_K/Ra_K = 0$ (a,c) and $Pe_K/Ra_K = 0.1$ (b,d).

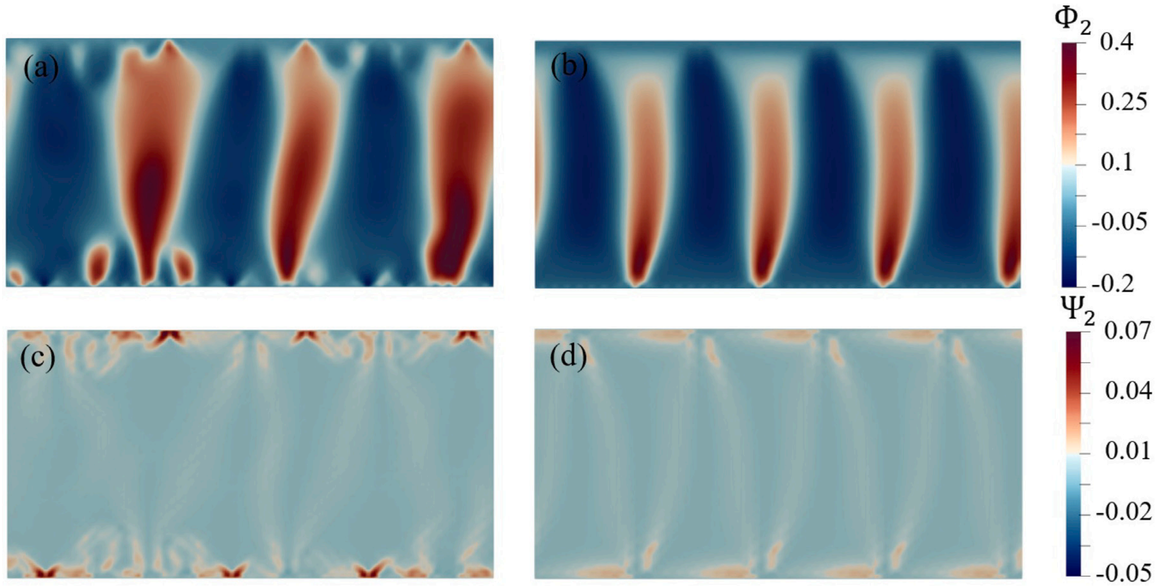

Fig. 16. Snapshots of the vertical macroscopic advection, Φ_1 (a,b), and vertical pore-scale dispersion, Ψ_1 (c,d), at $Ra = 1000$, comparing $Pe_K/Ra_K = 0$ (a,c) and $Pe_K/Ra_K = 0.1$ (b,d).

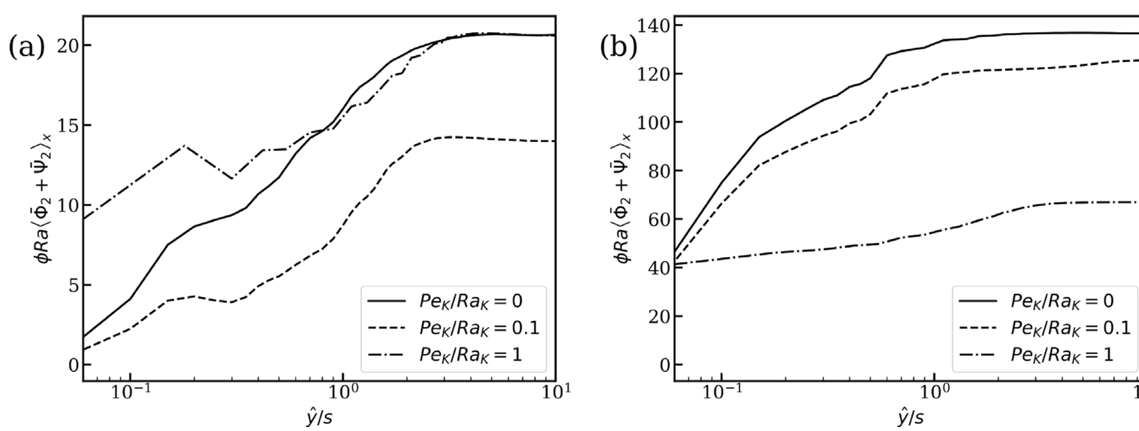

Fig. 17. Distribution of the horizontal-line- and time-averaged total vertical advection, $\langle\bar{\Phi}_2 + \bar{\Psi}_2\rangle_x$, as a function of the wall-normal coordinate for (a) $Ra = 1000$ and (b) $Ra = 20000$. Results are shown for $Pe_K/Ra_K = 0$, 0.1, and 1.

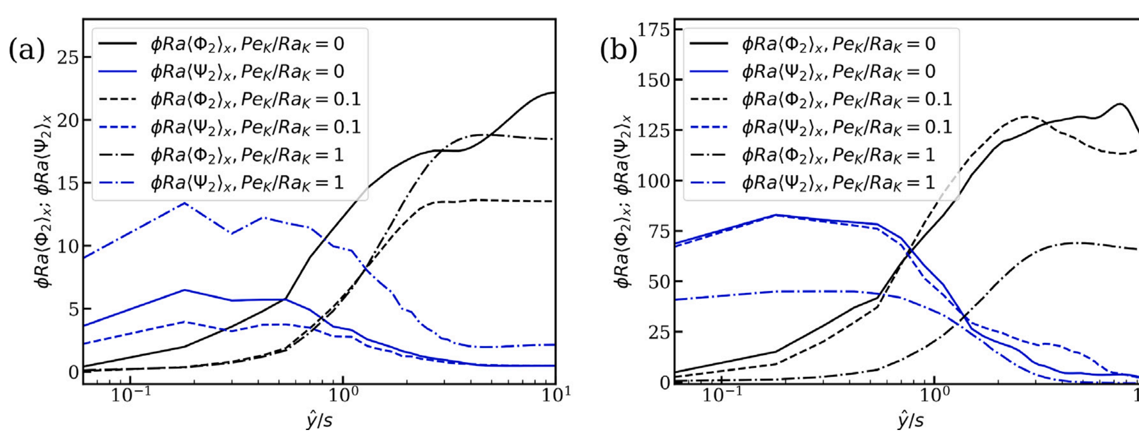

Fig. 18. Distribution of the horizontal-line-averaged transient macroscopic vertical advection $\langle\Phi_2\rangle_x$ and pore-scale dispersion $\langle\Psi_2\rangle_x$ as functions of wall-normal coordinate for $Ra = 1000$ (a) and 20000 (b). The results are shown for $Pe_K/Ra_K = 0$, 0.1 and 1.

three to five as Pe_K/Ra_K increases from 0 to 1. At a high Rayleigh number (Ra = 20000), the plume number increases from two to three (ϕ = 0.46) or three to five (ϕ = 0.56) as Pe_K/Ra_K increases from 0 to 0.1. However, as Pe_K/Ra_K increases further increases to 1, the plume

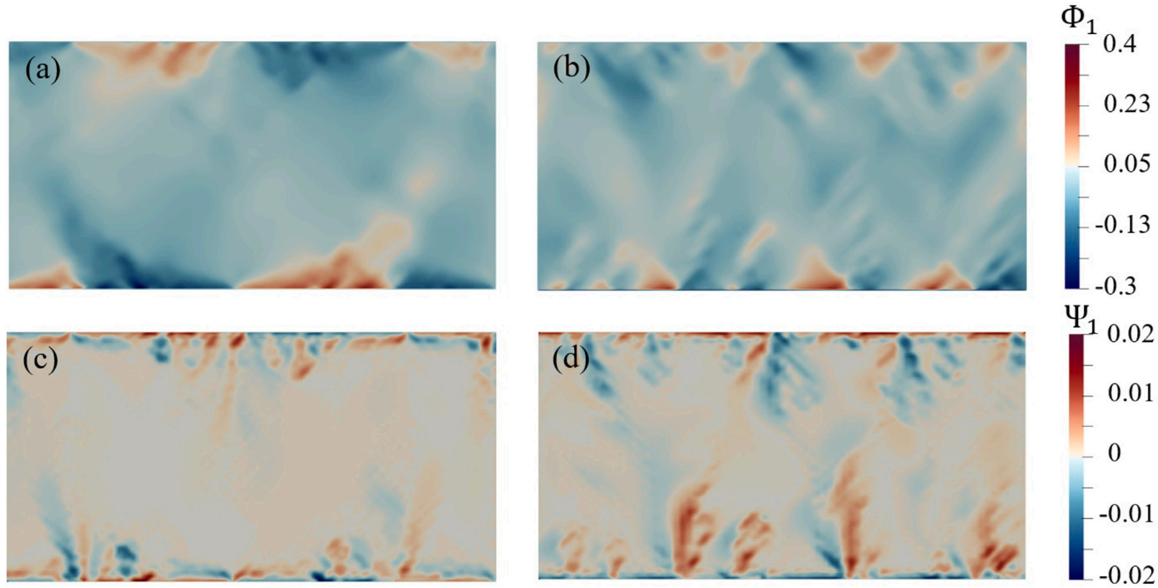

Fig. 19. Snapshots of the horizontal macroscopic advection, Φ_1 (a,b), and horizontal pore-scale dispersion, Ψ_1 (c,d), at Ra = 20000, comparing Pe_K/Ra_K = 0 (a,c) and $Pe_K/Ra_K = 0.1$ (b,d).

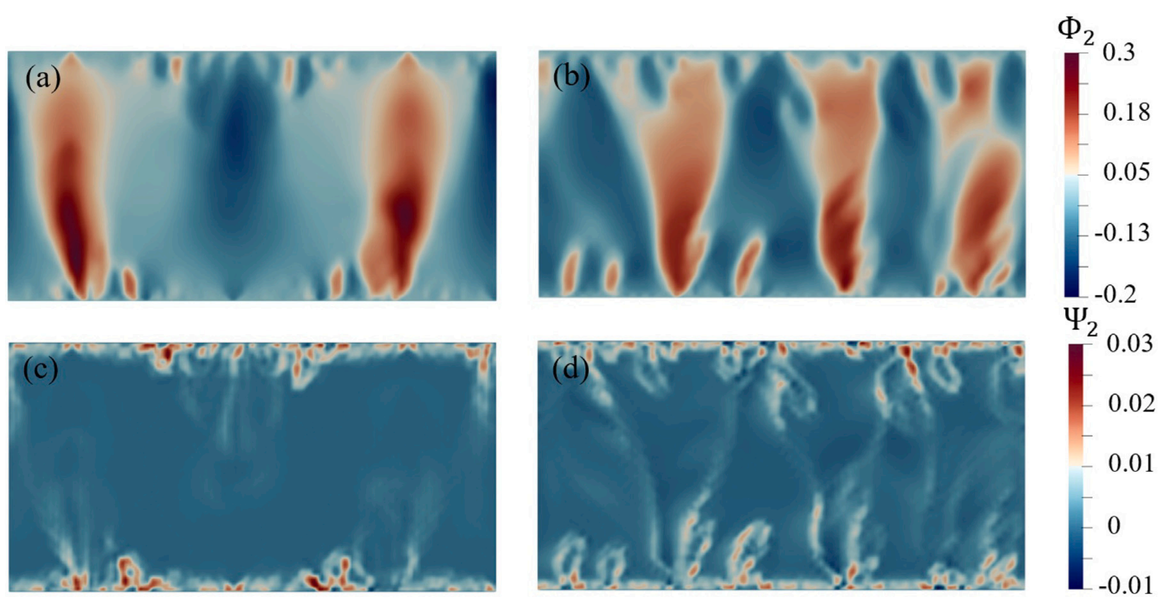

Fig. 20. Snapshots of the vertical macroscopic advection, Φ_1 (a,b), and vertical pore-scale dispersion, Ψ_1 (c,d), at $Ra = 20000$, comparing $Pe_K/Ra_K = 0$ (a,c) and $Pe_K/Ra_K = 0.1$ (b,d).

number decreases significantly to one (ϕ = 0.46) or two (ϕ = 0.56) since the horizontal dispersion introduced by the horizontal flow itself becomes significant.

As Pe_K/Ra_K increases at Ra = 1000 from 0 to 1, the temperature and velocity fluctuations $\hat{\theta}'$, $\hat{u}_1'$ and $\hat{u}_2'$ become stronger in the interior region. These fluctuations are partly due to the flow instabilities and partly due to plume transport in the horizontal direction when $Pe_K/Ra_K > 0$. The fluctuations reach their maximum value at Pe_K/Ra_K = 0.1 at Ra = 20000. Further increasing Pe_K/Ra_K to 1 reduces the fluctuations significantly. Increasing the porosity reduces the fluctuations in both pure natural convection and mixed convection cases, as it introduces stronger dispersion.

The horizontal flow has a complex effect on heat transfer. On the one hand, the reduced buoyancy-driven fluctuations weaken the vertical exchange between the wall region and the core region, reducing the vertical advection and pore-scale mechanical dispersion, leading to a lower Nusselt number. However, on the other hand, the weakened plume merging allows more proto-plumes to survive and develop into individual mega-plumes. The latter enhances the vertical advection and dispersion, thereby increasing the Nusselt number. This combined effect is apparent at $Ra = 1000$, where the "weakening" effect dominates and the Nusselt number decreases as Pe_K/Ra_K increases from 0 to 0.1. Then the "enhancing" effect dominates as Pe_K/Ra_K increases from 0.1 to 1. Similarly at Ra = 20000, as a result of these competing effects, the Nusselt number slightly decreases as Pe_K/Ra_K increases from 0 to 0.1. The Nusselt number decreases significantly as Pe_K/Ra_K increases from 0.1 to 1 since the horizontal dispersion caused by the horizontal flow gradually becomes dominant.

The DNS study demonstrates the significant impact of dispersion on mixed convection, a factor that cannot be overlooked in many engineering applications. The Nusselt numbers of the present DNS cases follow the scaling law $Nu \sim Ra^a$, where a = 0.5 for pure natural convection. For mixed convection with a fixed value of Pe_K/Ra_K, the exponent a decreases with increasing Pe. It can be approximated as $a = 0.5 - 2.5 \times 10^{-6} Pe$ according to the present DNS results. This means that, despite of the significant effect of the pore-scale dispersion on mixed convection, the effect of the horizontal flow on Nu can be approximated using the macroscopic Peclet number Pe.

Owing to the computational cost of pore-scale DNS, the present analysis is restricted to two-dimensional porous media with relatively simple geometries and a limited parameter range. The proposed scaling law is applicable to the conditions investigated in the present study. Its applicability beyond the examined parameter range remains to be validated and should therefore be interpreted with caution. The development of more general predictive correlations will require additional DNS, macroscopic simulations, and experimental investigations.

CRediT authorship contribution statement

Yan Jin: Writing – review & editing, Writing – original draft, Visualization, Validation, Supervision, Software, Resources, Project administration, Methodology, Investigation, Funding acquisition, Formal analysis, Data curation, Conceptualization. **Arne Speerforck:** Writing – review & editing, Supervision, Resources, Project administration, Conceptualization.

Declaration of competing interest

The authors declare that they have no known competing financial interests or personal relationships that could have appeared to influence the work reported in this paper.

Acknowledgments

The authors gratefully acknowledge financial support from the Deutsche Forschungsgemeinschaft (DFG, Grant No. 552151258). This work also benefited from the Excellence Cluster EXC 3120/1 BlueMat: Water-Driven Materials (Grant No. 533771286), funded by the DFG under the Excellence Strategy of the German Federal and State Governments. The computations were performed at the computing center of Hamburg University of Technology (RZ-TUHH) and at the Gesellschaft für Wissenschaftliche Datenverarbeitung mbH Göttingen (GWDG).

Data availability

The data are available through direct contact with the author.

References

[1] S.S. Jeffrey, T.V. Kalliat, J.T. Louis, Bubble column reactors for wastewater treatment. 1. theory and modeling of continuous countercurrent solvent sublation, Ind. Eng. Chem. Res. 35 (5) (1996) 1688–1699.
[2] H.E. Huppert, J.A. Neufeld, The fluid mechanics of carbon dioxide sequestration, Annu. Rev. Fluid Mech. 46 (2014) 255–272.
[3] S. Huang, M. Cao, L. Cheng, Experimental study on the mechanism of enhanced oil recovery by multi-thermal fluid in offshore heavy oil, Int. J. Heat Mass Transfer 122 (2018) 1074–1084.
[4] S.A. Ghoreishi-Madiseh, F.P. Hassani, A. Mohammadian, P.H. Radziszewski, A transient natural convection heat transfer model for geothermal borehole heat exchangers, J. Renew. Sustain. Energy 5 (4) (2013) 043104.
[5] M. Dehghan, M.S. Valipour, A. Keshmiri, S. Saedodin, N. Shokri, On the thermally developing forced convection through a porous material under the local thermal non-equilibrium condition, Int. J. Heat Mass Transfer 92 (2016) 815–823.
[6] F.C. Lai, F.A. Kulacki, The effect of variable viscosity on convective heat transfer along a vertical surface in a saturated porous medium, Int. J. Heat Mass Transfer 33 (1990) 1028–1031.
[7] A. Bidarmaghz, G.A. Narsilio, Is natural convection within an aquifer a critical phenomenon in deep borehole heat exchangers' efficiency? Appl. Therm. Eng. 212 (2022) 118450.
[8] N. Mehraeen, M.M. Ahmadi, O. Ghasemi-Fare, Numerical modeling of mixed convection near a vertical heat source in saturated granular soils, Geothermics 106 (2022) 102566.
[9] V.X. Tung, V.K. Dhir, Convective heat transfer from a sphere embedded in unheated porous media, ASME J. Heat Transf. 115 (1993) 503–506.
[10] T. Sano, K. Makizono, Unsteady mixed convection around a sphere in a porous medium at low péclet numbers, Fluid Dyn. Res. (1998).
[11] M. Combarnous, P. Bia, Combined free and forced convection in porous media, Soc. Pet. Eng. J. 11 (1971) 399–405.
[12] H. Chandra, Fluid flow and heat transfer due to differentially heated walls of horizontal channel filled with porous medium, J. Heat Mass Transf. 146 (12) (2024) 122601.
[13] A.K. Sharma, P. Bera, Linear stability of mixed convection in a differentially heated vertical channel filled with high permeable porous-medium, Int. J. Therm. Sci. 134 (2018) 622–638.
[14] D.A. Nield, A. Bejan, Convection in Porous Media, Springer, New York, 2017.
[15] F.C. Lai, F.A. Kulacki, Thermal dispersion effects on non-Darcy convection over horizontal surfaces in saturated porous media, Int. J. Heat Mass Transfer 32 (1989) 971–976.
[16] M.J.S. de Lemos, Turbulence in Porous Media, Modeling and Applications, second ed., Elsevier, Amsterdam, 2012.
[17] Y. Liu, H. Xiao, T. Aquino, M. Dentz, M. Wang, Scaling laws and mechanisms of hydrodynamic dispersion in porous media, J. Fluid Mech. 1001 (2024) R2.
[18] J.W. Elder, Steady free convection in a porous medium heated from below, J. Fluid Mech. 27 (1967) 29–48.
[19] D.R. Hewitt, J.A. Neufeld, J.R. Lister, Ultimate regime of high Rayleigh number convection in a porous medium, Phys. Rev. Lett. 108 (22) (2012) 224503.
[20] D.R. Hewitt, J.A. Neufeld, J.R. Lister, Convective shutdown in a porous medium at high Rayleigh number, J. Fluid Mech. 719 (2013) 551–586.
[21] D.R. Hewitt, J.A. Neufeld, J.R. Lister, High Rayleigh number convection in a three-dimensional porous medium, J. Fluid Mech. 748 (2014) 879–895.
[22] P.U. Kränzien, Y. Jin, Natural convection in a two-dimensional cell filled with a porous medium: A direct numerical simulation study, Heat Transf. Eng. 40 (5–6) (2019) 487–496.
[23] S. Gasow, A.V. Kuznetsov, Y. Jin, Prediction of pore-scale-property dependent natural convection in porous media at high Rayleigh numbers, Int. J. Therm. Sci. 179 (2022) 107635.
[24] P. Cheng, Natural convection in a porous medium: external flows, in: S. Kakac, W. Aung, R. Viskanta (Eds.), Natural Convection: Fundamentals and Applications, Hemisphere, Washington, DC, 1985, pp. 475–513.
[25] S. Kimura, A. Bejan, I. Pop, Natural convection near a cold plate facing upward in a porous medium, ASME J. Heat Transf. 107 (1985) 819–825.
[26] P. Cheng, I.D. Chang, On buoyancy induced flows in a saturated porous medium adjacent to impermeable horizontal surfaces, Int. J. Heat Mass Transfer 19 (1976) 1267–1272.
[27] C. Wang, M. Mobedi, A comprehensive pore scale and volume average study on solid/liquid phase change in a porous medium, Int. J. Heat Mass Transfer 159 (2020) 120102.
[28] A. Xu, B.R. Xu, H.D. Xi, Pore-scale statistics of temperature and thermal energy dissipation rate in turbulent porous convection, Phys. Rev. Fluids 8 (2023) 093504.
[29] E. Holzbecher, The mixed convection number for porous media flow, in: D.B. Ingham, A. Bejan, E. Mamut, I. Pop (Eds.), Emerging Technologies and Techniques in Porous Media, Kluwer Academic, Dordrecht, 2004, pp. 169–181.
[30] F.C. Lai, F.A. Kulacki, Effects of flow inertia on mixed convection along a vertical surface in a saturated porous medium, in: ASME Heat Transfer Division, HTD, vol. 96, (1) 1988, pp. 643–652.
[31] A. Nakayama, I. Pop, A unified similarity transformation for free, forced and mixed convection in Darcy and non-Darcy porous media, Int. J. Heat Mass Transfer 34 (1991) 357–367.
[32] H. Emami-Meybodi, Dispersion-driven instability of mixed convective flow in porous media, Phys. Fluids 29 (9) (2017) 094102.
[33] I. Michel-Meyer, U. Shavit, A. Tsinober, R. Rosenzweig, The role of water flow and dispersive fluxes in the dissolution of CO2 in deep saline aquifers, Water Resour. Res. 56 (11) (2020) e2020WR028184.
[34] A. Tsinober, R. Rosenzweig, H. Class, R. Helmig, U. Shavit, The role of mixed convection and hydrodynamic dispersion during CO_2 dissolution in saline aquifers: A numerical study, Water Resour. Res. 58 (2022) e2021WR030494.
[35] A. Xu, T.S. Zhao, L. Shi, J.B. Xu, Lattice Boltzmann simulation of mass transfer coefficients for chemically reactive flows in porous media, ASME J. Heat Transf. 140 (5) (2018) 052601.
[36] M.R. Islam, Evolution of oscillatory and chaotic flows in mixed convection in porous media in the non-Darcy regime, Chaos Solitons Fractals 2 (1992) 51–71.
[37] T.J. Chung, J.H. Park, C.K. Choi, D.Y. Yoon, The onset of vortex instability in a laminar forced convection flow through a horizontal porous channel, Int. J. Heat Mass Transfer 45 (2002) 3061–3064.

[38] T.J. Chung, M.C. Kim, C.K. Choi, The spatiotemporal instability of mixed convection in porous media, Korean J. Chem. Eng. 26 (2009) 332–338.
[39] S. Gasow, A.V. Kuznetsov, M. Avila, Y. Jin, A macroscopic two-length-scale model for natural convection in porous media driven by a species-concentration gradient, J. Fluid Mech. 926 (2021) A8.
[40] Y. Jin, A pore-scale resolved direct numerical simulation study for scaling analysis of the solutal convection in porous, J. Fluid Mech. 1000 (2024) A21.
[41] S. Gasow, Z. Lin, H. Zhang, A.V. Kuznetsov, M. Avila, Y. Jin, Effects of pore scale on the macroscopic properties of natural convection in porous media, J. Fluid Mech. 891 (2020) A25.
[42] D.J. Keene, R.J. Goldstein, Thermal convection in porous media at high Rayleigh numbers, ASME J. Heat Transf. 137 (3) (2015) 034503.
[43] D.A.G. Bruggeman, Calculation of various physics constants in heterogeneous substances. I. Dielectric constants and conductivity of mixed bodies from isotropic substances, Ann. Phys., Lpz. 24 (1935) 636–644.